# Modeling Damage and Damage Evolution in Periodic Cellular Sandwich Panels

by

Collins Ogundipe

A thesis submitted in conformity with the requirements
for the degree of Master of Applied Science
Graduate Department of Aerospace Science and Engineering
University of Toronto

# Abstract

Modeling Damage and Damage Evolution in Periodic Cellular Sandwich Panels

Collins Ogundipe
Master of Applied Science
Graduate Department of Aerospace Science and Engineering
University of Toronto
2012

Among the light bending structures currently available, truss core panels are one of the most efficient when properly designed. The proper selection of the truss core lattice allows the incorporation of additional functionality. But the structural complexity of the lattice makes prediction of the behavior of the panel more difficult, particularly in circumstances where the panel has been damaged. To exploit the advantages of truss core sandwich structures, it is therefore crucial to understand how the materials behave, degrade and survive in challenging environments. In this research, the strengths of truss core panels have been predicted based on their geometry and parent materials. Numerical calculations and experiments were carried out to validate the predicted strengths. The effects of damage and damage propagation on the overall strength of the panel were also addressed. In the numerical calculations, damage was inflicted on the panel by first loading an undamaged panel until a strut member fails in either yielding or buckling. The collapsed strut member is then removed (mimicking damage) and the macroscopic strength of the resulting panel is calculated. The strength and failure surfaces of arrays of partially damaged truss core unit cells are calculated under shear and axial loading. The results highlight the modes and trends of damage propagation in truss core panel, and the estimated strength of the panel in the damaged state. The predicted damaged strength of the panel were then compared with the strength measured in the damaged state experiments.

# Acknowledgements

First and foremost, I would like to express my gratitude to Professor Craig Steeves for giving me this research opportunity and the guidance in completing this thesis. His encouragements and suggestions have been tremendously helpful over the course of my research. I would also like to thank Professor Philippe Lavoie for being the second reader of this thesis. This research would not have been made possible without the support provided by Defence Research and Development Canada (DRDC). I would also like to thank Cellular Materials International (CMI), USA, for some of the testing samples they provided. Experimental equipment for the work in this thesis were made available in our lab by the funding provided by NSERC for their purchase. I would like to acknowledge their support for committing to upgrading the Multi-functional Structures Lab at the University of Toronto Institute for Aerospace Studies (UTIAS).

Last but not least, I would like to thank my family and friends for their help and encouragement in my studies. Special thanks go to my parents who have provided me with inspiration and unwavering support throughout my endeavours.

Collins Ogundipe
University of Toronto Institute for Aerospace Studies
February 3, 2012

# Contents

# Chapter 1

# Introduction

Structures including solid sheet or plate members are commonly seen in various engineering applications, being found in automobiles, buildings, aircraft, industrial equipment, and a host of other applications. Sheet and plate materials are quite strong and relatively inexpensive. Disadvantageously they tend to have a relatively low stiffness to weight ratio, notably in bending. Sandwich structures are frequently used in applications and implementations where it is desirable for structures to have a relatively high stiffness to weight ratio and/or where weight reduction is a significant factor. Such application is widely seen in structural material used in the aerospace industry. The most commonly used sandwich structure, typically referred to as honeycomb structure, includes thin face sheet laminates and a honeycomb core. Honeycomb sandwich structures have significantly higher stiffness to weight ratio than solid sheet or plate materials [1]. Disadvantageously, honeycomb structures tend to be limited to relatively thin face sheets. Further, honeycomb structures tend to be more expensive and difficult to manufacture when compared to truss core panels manufactured by laser welding because their manufacturing process typically involve complicated bonding procedures for attaching the honeycomb core to the face sheets. There are also difficulties with forming them into complex non-planar shapes due to induced anticlastic curvature [2].

Another sandwich structure, referred to as truss core sandwich panel, includes a corrugated sheet or a truss core disposed between two face sheets as shown in Figure 1.1

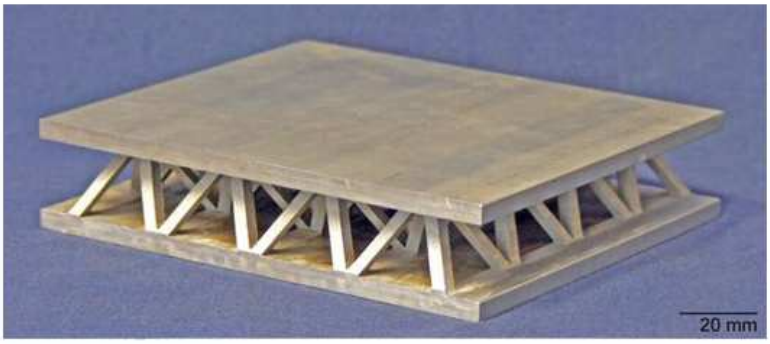


Figure 1.1: Model of an extruded/electrodischarge-machined pyramidal lattice sandwich structure.

Truss core sandwich panels also have significantly higher stiffness to weight than solid sheet or plate materials, although generally not as high as that of honeycomb structures [3]. But truss core sandwich panels tend to be advantageous for some applications as their open core architecture can be exploited for multi-functional applications. For instance, the open truss core could simultaneously be used as a structure and a heat transfer device. Also, the closed nature of the porosity of honeycomb structures can trap moisture leading to corrosion, while their skins are more susceptible to interfacial debonding. Open cell cores based upon truss core concepts allow fluids to pass through which makes them less susceptible to internal corrosion and depressurization induced delamination. When used as sandwich cores, they are more amenable to shaping into complex shapes. Moreover, the open core architecture can be exploited for providing attributes like impact energy absorption, thermal management, electromagnetic wave shielding, catalyst support, fluid filtering, or biological tissue in-growth [4, 5, 6, 7]. As such, lattice truss structures have been explored as more functional alternative cellular core topology [8, 9, 10]. Improved methods of manufacturing such sandwich panels have been developed for reducing the difficulties associated therewith and for producing robust, relatively inexpensive panels [11, 12]. Among the types of truss available are pyramidal, tetrahedral, octet-truss and Kagome. For the purpose of this study, a pyramidal lattice truss structure has been adopted. Pyramidal lattice truss structures are usually fabricated from high-ductility alloys by folding a perforated metal sheet along node rows. Recent work [13, 14] has shown that the pyramidal truss structure can be fabricated from an expanded-metal net. This method has a great advantage over the other methods since it requires the least material loss and uses a well-established process for expanded metals.

Conventional joining methods such as brazing or laser welding are then used to bond the core to solid face sheets to form a sandwich structure, efficiently eliminating the possible effects of poor joint design and ensuring adequate node-face sheet interfacial bonding [15]. The lattice topology, core relative density and parent alloy mechanical properties determine the mode of truss deformation and therefore the out-of-plane and in-plane mechanical properties of these structures. When sandwich panels are subjected to shear or bending loads, the nodes transfer forces from the face sheets to the core members (assuming adequate node bond strength and ductility exists) and the topology for a given core relative density dictates the load carrying capacity. Models for the stiffness and strength of pyramidal lattice truss cores, comprising elastic-plastic struts with perfect nodes, have been developed [16]. These models assumed that the trusses are pin-connected to rigid face sheets so that bending effects make no contribution to the stiffness and strength [17]. These models also assume the node strength to be the same as the strength of the parent metal alloy.

To utilize the advantages of truss core sandwich structures, current research on core structures focuses on optimizing the geometry and the materials to achieve better mechanical properties. Other factors such as corrosion, fatigue, blast resistance, and damage tolerance also contribute to their performance and possible failure during use. There is significant interest in exploring the various applications of truss core sandwich panels, especially in the design of military vehicles such as ships and aircraft. Owing to their complex damage behaviour, further research is crucial to understanding details of how the materials behave, degrade and survive in challenging environments. The scope of this research study involves analytical predictions of the strength and stiffness of the pyramidal truss core, analyzing the different modes of failure, and the failure criteria. A second key goal is the prediction of damage evolution during service. The research results highlight the numerical estimations of truss core panel damaged state strength in a normalized stress space, the trend of damage propagation and experimental validations of the predicted damaged strength.

# Chapter 2

# Analytical Predictions and Numerical Calculations

## 2.1 Derivation of Analytical Expressions

### 2.1.1 Basic Assumptions

The collapse response of stretching-dominated unit cells under transverse shear and normal loading has been explored. The unit cells are pyramidal trusses with squared face sheets, as shown in Figure 2.1, comprising elastic-plastic, circular cylindrical struts of length $l$ and radius $a$, making an angle $\omega$ with the face sheet. The struts are pin-jointed at the nodes. The unit cells are *stretching-dominated* [17] because the structural loads are carried by elements of the unit cells only through axial forces, without bending, and the structure collapses by axial yielding or buckling of the struts. The effective moduli and failure strength of the trusses are calculated by assuming that the aspect ratio $(a/l)$ for strut is small. It is assumed that the pin-jointed struts are made of elastic-ideally plastic solid, which is made of the same material as the face sheets.

Figure 2.1: Unit cell pyramidal truss sandwich made of circular cylindrical struts. Figure courtesy of John Hwang.

### 2.1.2 Representative Model and Modes of Loading

In pure shear or pure normal loading, the stresses in each of the struts in any unit cell are assumed to be equal in magnitude; the struts are subjected to loading in tension or compression. Because the function of the truss core sandwich panel is to carry normal and shear loads, the focus is on the normal stresses in the $X_3$-direction (out-of-plane axis) and the transverse shear stresses in $X_1$ or $X_2$ direction which, by symmetry, are equivalent. Since the pyramidal geometry is regular with equal sides and angles, and the truss members are of the same thickness, it can be concluded that there is sufficient symmetry for the transverse shear modulus of the core to be independent of the orientation within the $X_1$-$X_2$ plane. Two independent elastic moduli are denoted by $E_{33}$ for the Young's modulus and $G_{13}$ for the shear modulus. The modulus $G_{13} = G_{23}$, as the in-plane properties do not depend on the direction of loading. The possible failure modes and corresponding failure surfaces are detailed in the subsequent sections.

As shown in Figure 2.2, the normal loading in the $X_3$-direction is represented by applying a point force $F_3$ to the apex node A of the single-unit pyramidal truss. The force $F_3$ exerts a tensile (or compressive) stress $\sigma_{33}$ on the pyramidal unit cell, with the force scaled to the area of the load-bearing section of the unit cell. This area of the load-bearing section is calculated by finding the area of the pyramidal base, denoted by $A_{base}$. From Figure 2.3, the horizontal component of the length of the strut is calculated to be $l\cos\omega$, and the length of each side of the squared pyramidal base can be calculated

as $\sqrt{2}l\cos\omega$, resulting in a base area of $2l^2\cos^2\omega$.

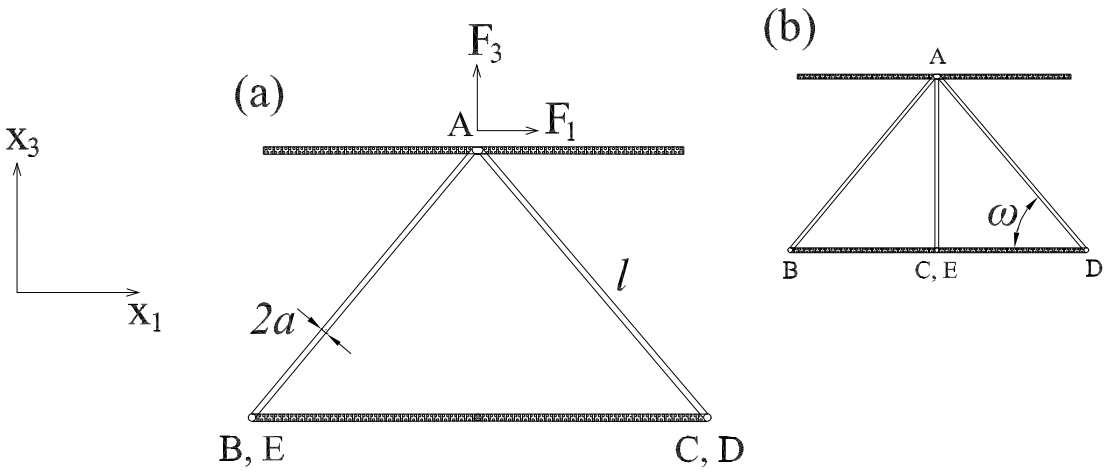


Figure 2.2: (a) Pyramidal unit cell showing the front view of the pyramidal core geometry with the circular struts (AB,AC,AD,AE) subjected to loading by the nodal forces applied at the node A. (b) The unit cell rotated 45°.

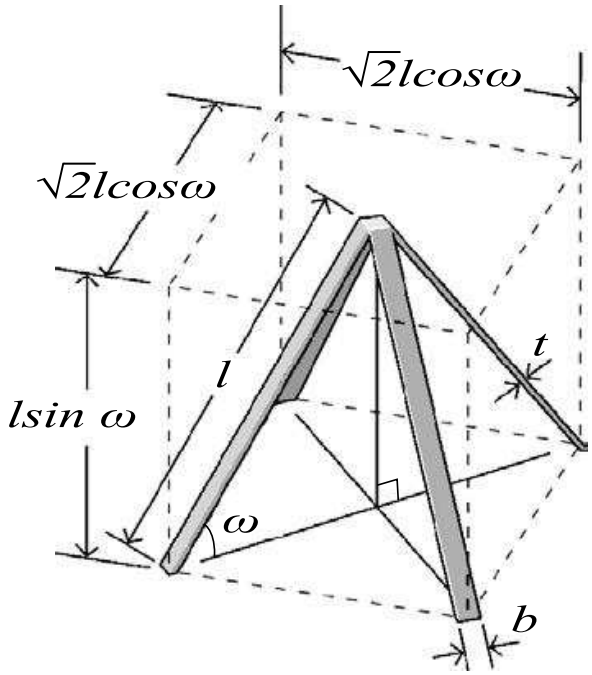


Figure 2.3: Unit cell core geometry and parameters of a strut with rectangular cross-sections

The normal modulus $E_{33}$ can be found by calculating the normal displacements of

the two face sheets due to direct compression. Loading in the direction of $X_1$ or $X_2$ by the forces $F_1$ and $F_2$ as shown in Figure 2.4 result in stresses denoted $\sigma_{13}$ and $\sigma_{23}$ respectively, which are related to the transverse shear moduli $G_{13}$ and $G_{23}$.

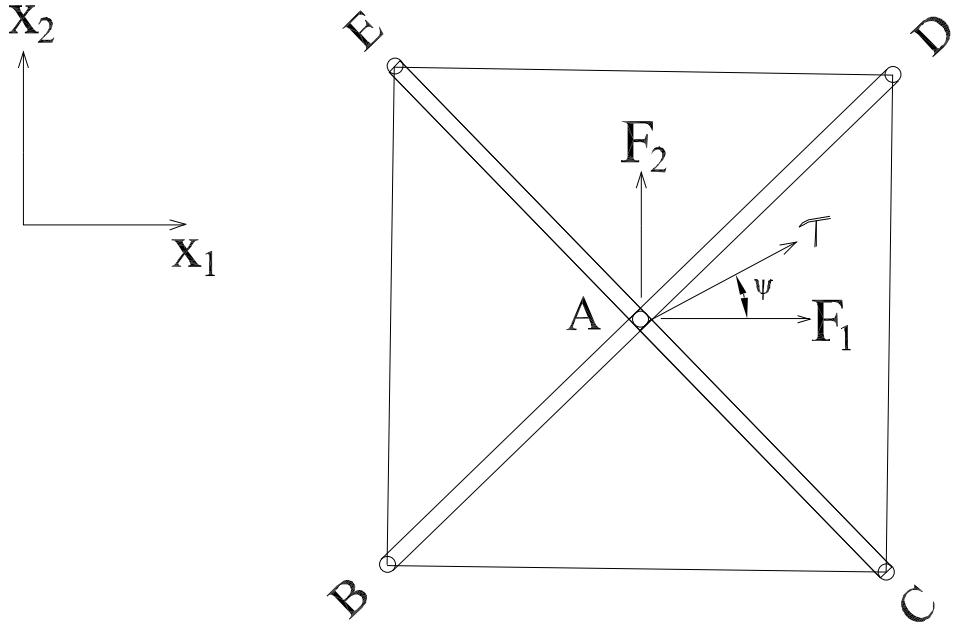


Figure 2.4: Top view of the pyramidal core geometry with the struts subjected to loading under the shear forces applied at the node A.

### 2.1.3 Analytical Predictions of Strength

The relative density, $\bar{\rho}$, of the sandwich panel core is an important property of truss-cored sandwich panels. The relative density of the pyramidal truss core (defined by the density of the core divided by the density of the solid from which the core is made) is

$$\bar{\rho} = \frac{\rho_c}{\rho_s},$$

where $\rho_c$ is the average density of the core region and $\rho_s$ is the density of the parent solid material. Taking the volume of the core as $V_c$ and that of the struts as $V_s$, the relative density for a core with circular cylindrical struts becomes

$$\bar{\rho} = \frac{2\pi}{\cos^2\omega \sin\omega} \left(\frac{a}{l}\right)^2, \tag{2.1}$$

with the height of the core given by $l \sin\omega$, which is the vertical component of the strut length. Considering a single strut member under the application of normal force component $F_3$ (corresponding to the applied stress $\sigma_{33}$), the force in the single strut member is $F_{strut}$,

$$F_{strut} = \frac{\sigma_{33} A_{base}}{4 \sin\omega}.$$

The collapse of the unit cell may occur by strut yielding in tension or compression, or by strut buckling. The failure of the strut will occur when the stresses induced in the unit cell struts, $\sigma_s$, due to applied stresses $\sigma_{33}$, $\sigma_{13}$ and $\sigma_{23}$ exceed the material yield strength, $\sigma_y$, or the critical strength, $\sigma_{cr}$, in the case of buckling. As a result, yielding will occur when

$$\left| \frac{F_{strut}}{A_{strut}} \right| = |\sigma_s| = \sigma_y, \tag{2.2}$$

where $A_{strut}$ is the cross-sectional area of the strut ($\pi a^2$ for circular struts). For clarity, $\sigma_s$ is the stress resulting from the axial forces induced in the strut members as a result of the external applied stresses ($\sigma_{33}$ in compression and $\sigma_{13}$–$\sigma_{23}$ in shear). In the case of pure normal loading for a truss core made of circular struts, yielding follows as below:

$$\begin{aligned} \sigma_y \pi a^2 &= \frac{\sigma_{33} A_{base}}{4 \sin\omega}, \\ \sigma_{33} &= \sigma_y \sin^2\omega \bar{\rho}. \end{aligned} \tag{2.3}$$

For the case of buckling, failure will occur when

$$\sigma_s = -\sigma_{cr} \equiv -\frac{F_{cr}}{A_{strut}},$$

where $F_{cr}$ is given as

$$F_{cr} = \frac{k^2 \pi^2 E_s I}{l^2}, \quad I = (1/4) a^4 \pi.$$

As a result,

$$\sigma_s = -\sigma_{cr} \equiv -\frac{k^2 \pi^2 E_s a^2}{4 l^2}, \tag{2.4}$$

where $E_s$ is the Young's modulus of the constituent material from which the struts are made. The strength in buckling, $\sigma_{cr}$, is derived from the Euler buckling equation, and by taking $k = 1$ for pin-jointed elements.

For transverse shear under the application of shear force component $F_1$ and $F_2$ as shown in Figure 2.4, the transverse shear strength shall be specified in terms of the magnitude of shear stress $\tau$ and its direction $\psi$ with respect to $X_1$ axis. Thus,

$$\sigma_{13} = \tau \cos\psi \,,\ \sigma_{23} = \tau \sin\psi.$$

Equilibrium dictates the relationship between forces $F_1$, $F_2$ on the node A and macroscopic shear stress $\tau$, such that

$$F_1 = A_{base}\sigma_{13},\ F_2 = A_{base}\sigma_{23}.$$

Consequently, for the case of pure shear under loading in $X_1$ direction, where $\psi = 0$;

$$F_{strut} = \frac{\tau A_{base}}{4\cos\omega\cos 45^\circ}.$$

For yielding to occur;

$$\begin{aligned} \frac{F_{strut}}{A_{strut}} &= \sigma_s = \sigma_y, \\ \sigma_y \pi a^2 &= \frac{\sigma_{13} A_{base}}{4\cos\omega\cos 45^\circ}, \\ \sigma_{13} &= \frac{1}{2\sqrt{2}}\sigma_y \sin 2\omega\bar{\rho}. \end{aligned} \tag{2.5}$$

Depending on the directions of the applied stresses to which a strut is subjected to, the stresses induced in the strut, $\sigma_s$, due to applied $\sigma_{13}$, $\sigma_{23}$ and $\sigma_{33}$, is:

$$\sigma_s = \left( \frac{\sigma_{33}}{\sin^2\omega} + \frac{2\sqrt{2}\sigma_{13}}{\sin 2\omega} + \frac{2\sqrt{2}\sigma_{23}}{\sin 2\omega} \right) \frac{1}{\bar{\rho}} \,. \tag{2.6}$$

A differential applied force d$F$ (related to stresses d$\sigma$) in the direction of a required displacement induces a change in the core height, d$h$:

$$dh = d\sigma \frac{2l^3\cos^2\omega}{4\sin^3\omega\pi a^2 E_s},$$

where h is the height of the unit cell, given by $l\sin\omega$. Using the above equation, the change in strain, $d\varepsilon$, becomes;

$$d\varepsilon = d\sigma \frac{2l^2\cos^2\omega}{4\sin^3\omega\pi a^2 E_s},$$

$$E = \frac{4\sin^3\omega\pi a^2 E_s}{2l^2\cos^2\omega},$$

where $E$ is the resulting normal modulus of the truss core. With respect to the normal direction $X_3$ axis, modulus $E_{33}$ becomes

$$\frac{E_{33}}{E_s} = \bar{\rho}\sin^4\omega.$$

Having established that the shear modulus $G_{13}$=$G_{23}$, the shear modulus can be deduced by applying the point load $F_1$ or $F_2$, and by determining the corresponding displacement. In an approach similar to the solution of $(E_{33}/E_s)$,

$$\frac{G_{13}}{E_s} = \frac{\bar{\rho}}{8}\sin^2 2\omega. \tag{2.7}$$

## 2.2 Failure Modes and Failure Surfaces

This section describes the different failure modes of the pyramidal truss core sandwich panel and the associated failure surfaces. A failure surface is a representation of an infinite number of failure points represented in a two or three-dimensional space of stresses. The failure point is defined as the stress at which the material begins to deform plastically. In this section, the failure surface is represented in a two-dimensional stress-space. The two axes are the normal stresses on the vertical axis and shear stresses on the horizontal axis for combined loading in $\sigma_{33}$–$\sigma_{13}$ space, and shear stresses on both axes for loading in $\sigma_{13}$–$\sigma_{23}$ space. The axes are normalized such that the vertices on the yielding surface are at $\pm 1$. The surfaces in the normalized stress space consist of points for each possible collapse under any applied ratio of the stresses on the axes. The surface must be convex and the state of stress inside the surface is elastic. The relationship between the applied stresses and the induced stresses is a linear function of the geometric parameter $(a/l)^2$, while additional trigonometric and constant terms are necessary to account for the angles of the struts.

As shown in Figure 2.5, the arrows on the struts in the depicted modes of failure denote stresses in either compression or tension. Compression is shown with the two arrows pointing toward each other, while struts in tension are represented with the arrows pointing away from each other. Struts failing by compression could either yield or buckle.

To understand the behavior of truss core structures with respect to different loading mechanisms, it is necessary to account for all the possible failure modes, and to generate corresponding failure surfaces. Mode [A] represents collapse in pure compression or tension. In this failure mode, all four struts are equally loaded and simultaneously yield (in tension or compression) or simultaneously buckle in compression. If $\sigma_{cr} < \sigma_y$, then buckling modes of failure are operative; the failure surface lies upon the dashed lines in Figure 2.6. Otherwise, the failure surface lies only upon the solid lines. In Mode [B], two struts yield in tension and their opposing struts yield in compression. This failure mode will occur only in pure shear. In Mode [C], two adjacent struts buckle in either pure shear or combined loading while the other two struts remain loaded but undamaged. Mode [D] denotes failure by simultaneous tensile yield of two struts and buckling of the two opposing struts under combined loading. The fifth mode of failure denoted as Mode [E] encompasses all the yielding failures in the combined loading ($\sigma_{13}$,$\sigma_{33}$). This mode involves the yielding of two adjacent struts in tension. In all failure modes, the unfailed strut members may be in tension or compression.

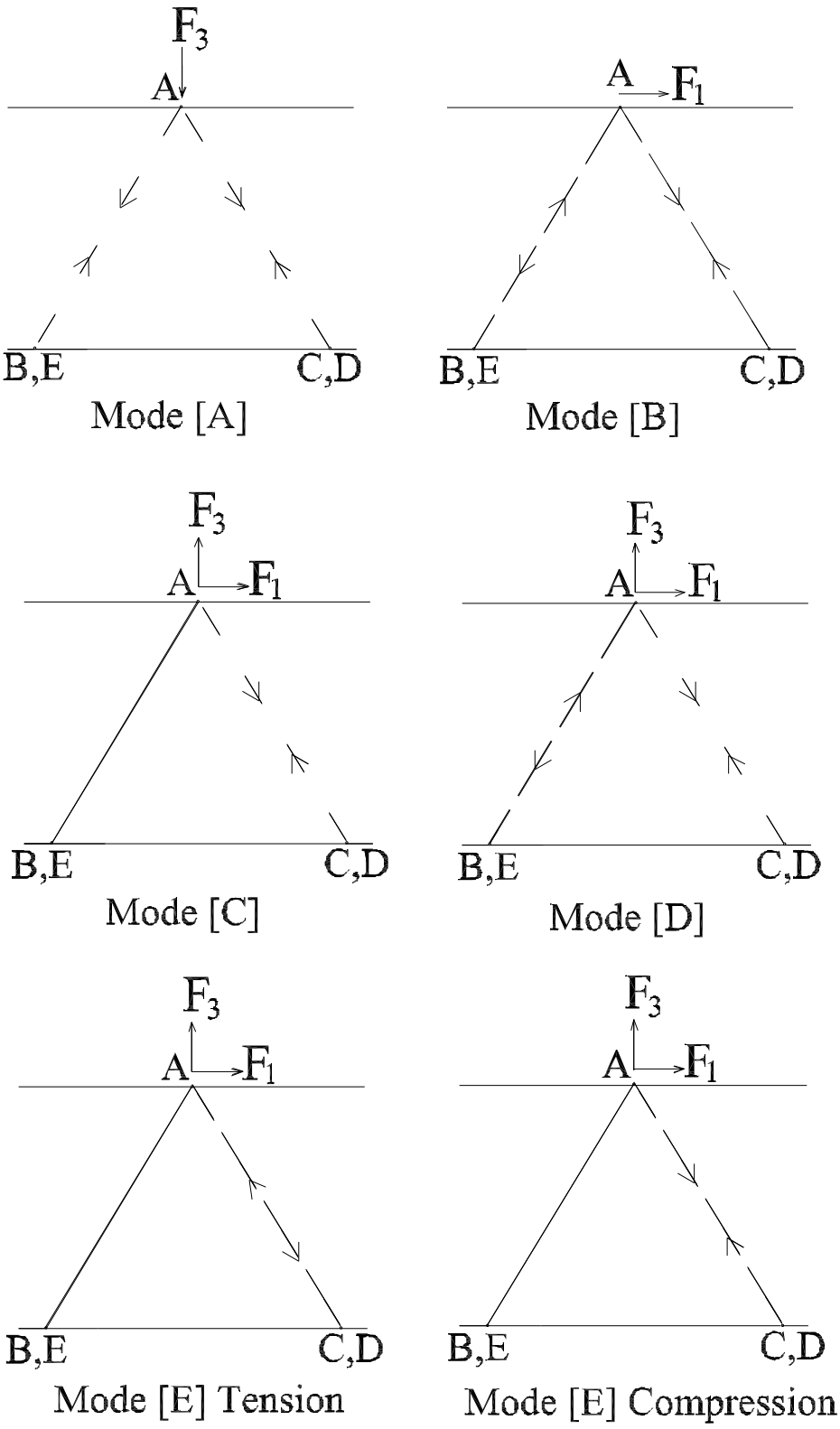


Figure 2.5: Mode [A] represents simultaneous collapse of all the struts under normal loading. Mode [B] represents the case of one strut yielding in tension while its opposing strut yields in compression. Mode [C] represents the case of two adjacent struts buckling. Mode [D] denotes simultaneous tensile yield of two struts and buckling of the two opposing struts under combined loading. Mode [E] represents the case of two adjacent struts yielding.

The yield and buckling failure surfaces represented in Figure 2.6 show the combined loading in ($\sigma_{13}$,$\sigma_{33}$) normalized stress space, while Figure 2.7 represents transverse shear in ($\sigma_{13}$,$\sigma_{23}$) normalized stress space. In the failure surfaces, the loading direction, $\gamma$, dictates the ratio of the vertical normalized stress to the horizontal component. When the loading point in the stress space is within the failure surface, the unit cell is undamaged. Damage corresponds with the lines on the failure surfaces, while the panel remain at its initial strength only within the enclosed failure surfaces. The loading point can never move outside the failure surface.

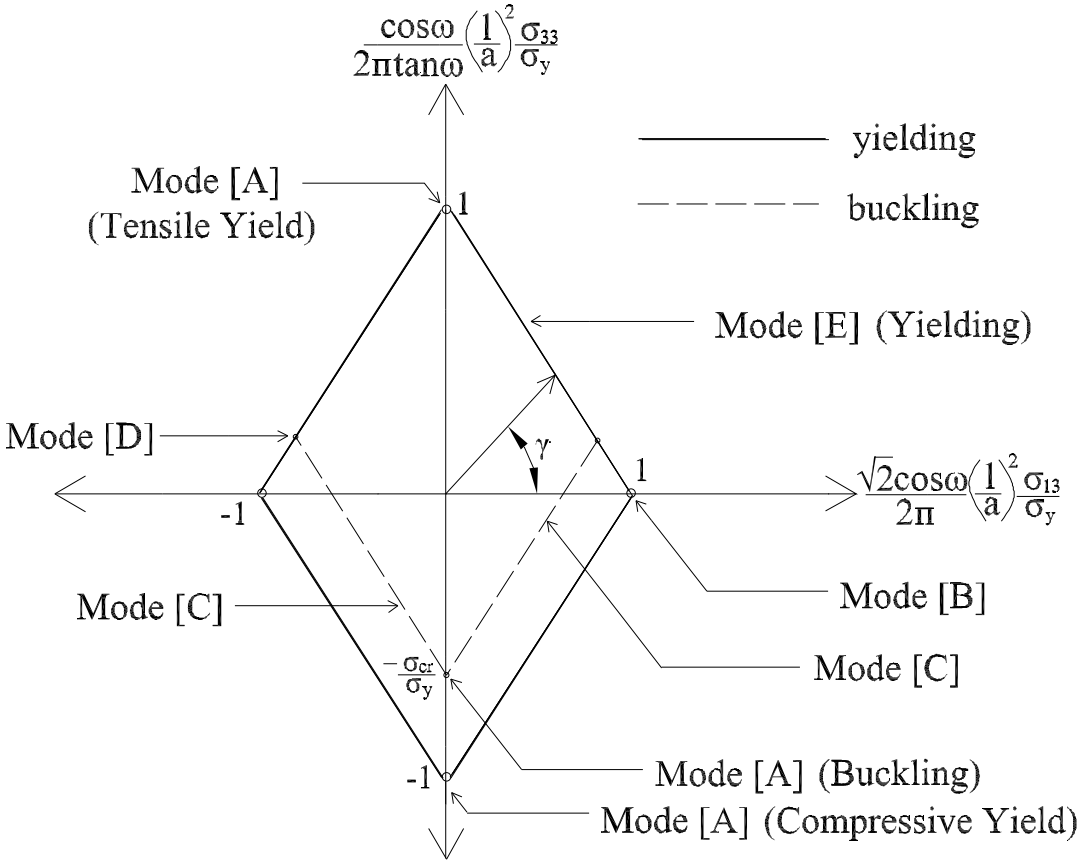


Figure 2.6: Yield and buckling failure surfaces in combined loading ($\sigma_{13}$,$\sigma_{33}$) space. The failure modes have only been partially labelled, the unlabelled collapse planes follow from symmetry.

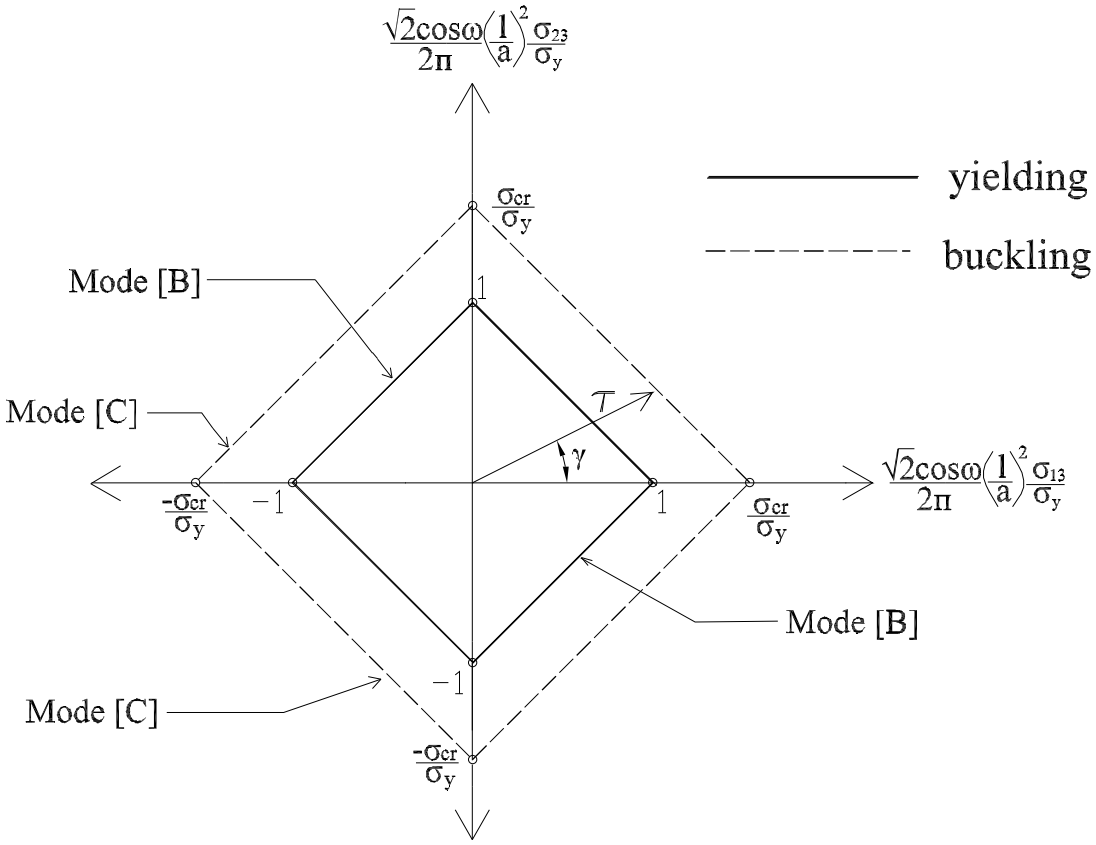


Figure 2.7: Yield and buckling failure surfaces in transverse shear. The failure modes have only been partially labeled, the unlabeled collapse planes follow from symmetry

Also, based on the geometry of the truss core sandwich panel, a non-dimensional strength of the panel can be expressed in terms of the ratio $(\sigma_{33}/\sigma_y)$ for normal stresses in the vertical axis and for the non-dimensional shear strength in the horizontal axis by the ratio $(\sigma_{13}/\sigma_y)$.

## 2.3 Numerical Calculation and Stiffness Matrix Approach

Owing to the need to study the behavior of the truss core sandwiches beyond just a single unit cell, as the real structure exists as large arrays of multiple unit cells, it is necessary to devise a method for analyzing the strength of such large array panel. Moreover, of major importance is the effect of the interactions between the unit cells on

the macroscopic strength of the panel. Using the stiffness method of matrix analysis, a MATLAB program was written for analyzing the strength and mechanical behavior of any multiple-cell truss core sandwich panel. With reference to the single truss member shown in Figures 2.8, a $x$,$y$,$z$ global coordinate system was established. The two nodal ends of the strut are identified as the near end, $N$, and the far end, $F$.

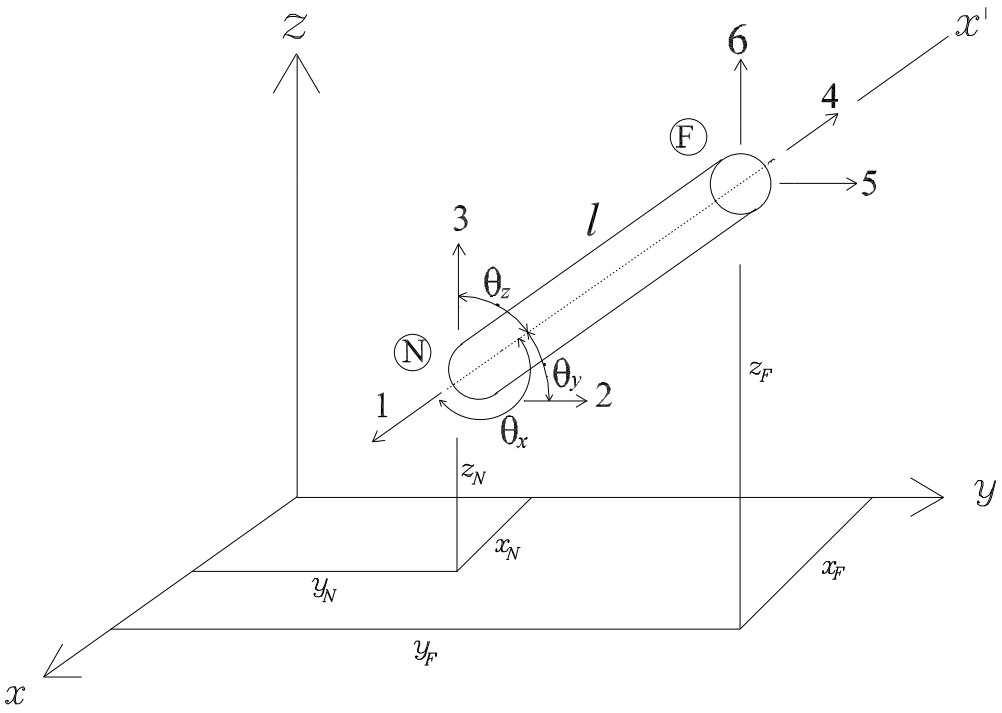


Figure 2.8: Single strut representation in space. Space truss analysis

Three degrees of freedom at the near end are labeled 1, 2, and 3, while the degrees of freedom at the far end are labeled 4, 5 and 6. The element stiffness matrix for the single truss member, $k'$, defined in reference to its local coordinates $x'$ is given by [18];

$$k' = \frac{AE}{l}\begin{bmatrix} \mathbf{1} & \mathbf{-1} \\ \mathbf{-1} & \mathbf{1} \end{bmatrix}$$

where $A$ denotes the area of the strut, $l$ is the strut length, and $E$ is the Young's modulus. The direction cosines $\lambda_x$, $\lambda_y$, $\lambda_z$ between the global and local coordinates can be found using the equations

$$\lambda_x = \frac{x_F - x_N}{\sqrt{(x_F - x_N)^2 + (y_F - y_N)^2 + (z_F - z_N)^2}}$$

$$\lambda_y = \frac{y_F - y_N}{\sqrt{(x_F - x_N)^2 + (y_F - y_N)^2 + (z_F - z_N)^2}}$$

$$\lambda_z = \frac{z_F - z_N}{\sqrt{(x_F - x_N)^2 + (y_F - y_N)^2 + (z_F - z_N)^2}}$$

The transformation matrix $T$ is given by

$$T = \begin{bmatrix} \boldsymbol{\lambda_x} & \boldsymbol{\lambda_y} & \boldsymbol{\lambda_z} & \mathbf{0} & \mathbf{0} & \mathbf{0} \\ \mathbf{0} & \mathbf{0} & \mathbf{0} & \boldsymbol{\lambda_x} & \boldsymbol{\lambda_y} & \boldsymbol{\lambda_z} \end{bmatrix}$$

The single truss member stiffness matrix expressed in the global coordinates with respect to the transformation matrix is given by

$$k = \begin{bmatrix} \boldsymbol{\lambda_x} & \mathbf{0} \\ \boldsymbol{\lambda_y} & \mathbf{0} \\ \boldsymbol{\lambda_z} & \mathbf{0} \\ \mathbf{0} & \boldsymbol{\lambda_x} \\ \mathbf{0} & \boldsymbol{\lambda_y} \\ \mathbf{0} & \boldsymbol{\lambda_z} \end{bmatrix} \frac{AE}{l} \begin{bmatrix} \mathbf{1} & \mathbf{-1} \\ \mathbf{-1} & \mathbf{1} \end{bmatrix} \begin{bmatrix} \boldsymbol{\lambda_x} & \boldsymbol{\lambda_y} & \boldsymbol{\lambda_z} & \mathbf{0} & \mathbf{0} & \mathbf{0} \\ \mathbf{0} & \mathbf{0} & \mathbf{0} & \boldsymbol{\lambda_x} & \boldsymbol{\lambda_y} & \boldsymbol{\lambda_z} \end{bmatrix}$$

Carrying out the matrix multiplication yields the symmetric matrix;

$$k = \frac{AE}{l} \begin{bmatrix} \boldsymbol{\lambda_x^2} & \boldsymbol{\lambda_x\lambda_y} & \boldsymbol{\lambda_x\lambda_z} & -\lambda_x^2 & \boldsymbol{-\lambda_x\lambda_y} & \boldsymbol{-\lambda_x\lambda_z} \\ \boldsymbol{\lambda_y\lambda_x} & \boldsymbol{\lambda_y^2} & \boldsymbol{\lambda_y\lambda_z} & \boldsymbol{-\lambda_y\lambda_x} & \boldsymbol{-\lambda_y^2} & \boldsymbol{-\lambda_y\lambda_z} \\ \boldsymbol{\lambda_z\lambda_x} & \boldsymbol{\lambda_z\lambda_y} & \boldsymbol{\lambda_z^2} & \boldsymbol{-\lambda_z\lambda_x} & \boldsymbol{-\lambda_z\lambda_y} & \boldsymbol{-\lambda_z^2} \\ \boldsymbol{-\lambda_x^2} & \boldsymbol{-\lambda_x\lambda_y} & \boldsymbol{-\lambda_x\lambda_z} & \lambda_x^2 & \boldsymbol{\lambda_x\lambda_y} & \boldsymbol{\lambda_x\lambda_z} \\ \boldsymbol{-\lambda_y\lambda_x} & \boldsymbol{-\lambda_y^2} & \boldsymbol{-\lambda_y\lambda_z} & \boldsymbol{\lambda_y\lambda_x} & \boldsymbol{\lambda_y^2} & \boldsymbol{\lambda_y\lambda_z} \\ \boldsymbol{-\lambda_z\lambda_x} & \boldsymbol{-\lambda_z\lambda_y} & \boldsymbol{-\lambda_z^2} & \boldsymbol{\lambda_z\lambda_x} & \boldsymbol{\lambda_z\lambda_y} & \boldsymbol{\lambda_z^2} \end{bmatrix}$$

To generate the structural stiffness matrix, $K$, for any given type of truss structure with the members' connectivity, positions and geometry defined, the elements of each member stiffness matrix are generated and placed directly into their respective positions in K in

the appropriate rows and columns. After the structural stiffness matrix ($K$) has been generated, the nodal displacements ($D$), external force reactions ($Q$) and internal member forces ($q$) can be determined in the form of equation $Q = KD$;

$$\begin{bmatrix} \mathbf{Q_k} \\ \mathbf{Q_u} \end{bmatrix} = \begin{bmatrix} \mathbf{K_{11}} & \mathbf{K_{12}} \\ \mathbf{K_{21}} & \mathbf{K_{22}} \end{bmatrix} \begin{bmatrix} \mathbf{D_u} \\ \mathbf{D_k} \end{bmatrix}$$

where $Q_k$ and $D_k$ are known external loads and displacements respectively. $Q_u$ and $D_u$ are the unknown loads and displacements, and $K$ is the structure stiffness matrix which is partitioned to be compatible with the partitioning of $Q$ and $D$. Most often $D_k$=0, since the supports are not displaced. Solving the above equations, for $D_k$=0, the direct solution for all the unknown nodal displacements can be obtained:

$$D_u = \begin{bmatrix} \mathbf{K_{11}} \end{bmatrix}^{-1} \begin{bmatrix} \mathbf{Q_k} \end{bmatrix}$$

and the solution for the unknown support reactions give as below;

$$Q_u = \begin{bmatrix} \mathbf{K_{21}} \end{bmatrix} \begin{bmatrix} \mathbf{D_u} \end{bmatrix}$$

The member forces can be determined using the equation

$$q = k'TD$$

Expanding this equation yields

$$\begin{bmatrix} \mathbf{q_N} \\ \mathbf{q_F} \end{bmatrix} = \frac{AE}{l} \begin{bmatrix} \mathbf{1} & \mathbf{-1} \\ \mathbf{-1} & \mathbf{1} \end{bmatrix} \begin{bmatrix} \lambda_\mathbf{x} & \lambda_\mathbf{y} & \lambda_\mathbf{z} & \mathbf{0} & \mathbf{0} & \mathbf{0} \\ \mathbf{0} & \mathbf{0} & \mathbf{0} & \lambda_\mathbf{x} & \lambda_\mathbf{y} & \lambda_\mathbf{z} \end{bmatrix} \begin{bmatrix} \mathbf{D_{Nx}} \\ \mathbf{D_{Ny}} \\ \mathbf{D_{Nz}} \\ \mathbf{D_{Fx}} \\ \mathbf{D_{Fy}} \\ \mathbf{D_{Fz}} \end{bmatrix}$$

Since $q_N = q_F$ for equilibrium, the solution can be written as;

$$q_F = \frac{AE}{l} \begin{bmatrix} -\lambda_{\mathbf{x}} & -\lambda_{\mathbf{y}} & -\lambda_{\mathbf{z}} & \lambda_{\mathbf{x}} & \lambda_{\mathbf{y}} & \lambda_{\mathbf{z}} \end{bmatrix} \begin{bmatrix} \mathbf{D_{Nx}} \\ \mathbf{D_{Ny}} \\ \mathbf{D_{Nz}} \\ \mathbf{D_{Fx}} \\ \mathbf{D_{Fy}} \\ \mathbf{D_{Fz}} \end{bmatrix}$$

If the computed result using the above equation is negative, the members are regarded to be in compression. This procedure was implemented using a series of MATLAB scripts [19], which was then used to calculate the strength and the failure surfaces of a unit pyramidal truss panel. For the purpose of comparing the analytical calculation of strength with that of the stiffness matrix approach, a unit pyramidal cell was chosen with strut length $l$=27.5 mm, radius $a$ of 0.69 mm, angle made by strut with face sheet $\omega$=55°, with Young's modulus $E$ of 69 GPa and yield strength $\sigma_y$ of 255 MPa. Figure 2.9 shows the failure surfaces for a unit cell subject to combined loading in the ($\sigma_{13}$,$\sigma_{33}$) stress space.

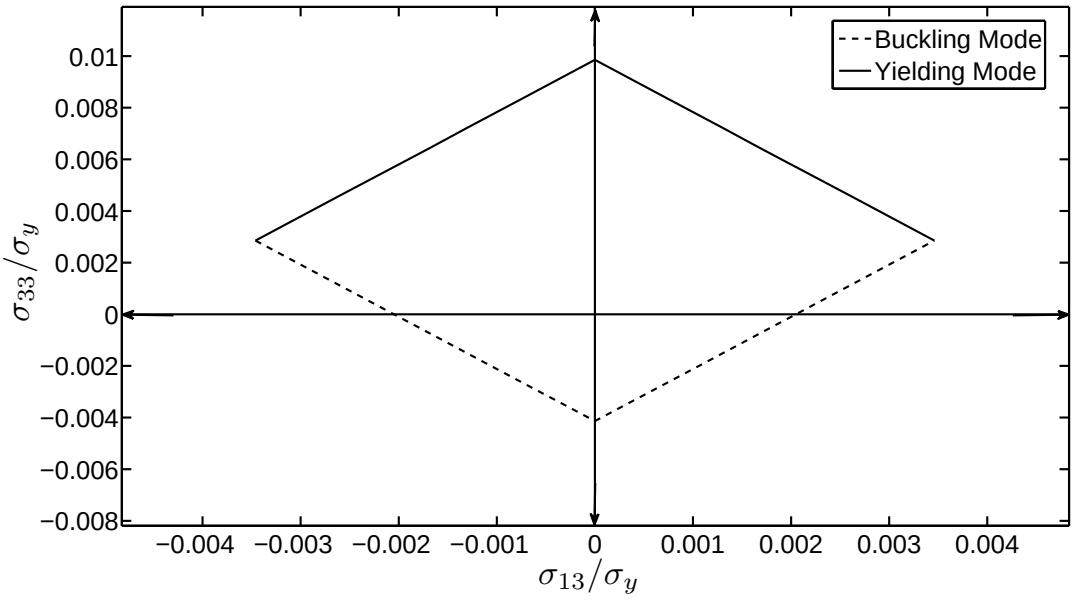


Figure 2.9: Numerically generated yield and buckling failure surfaces in combined loading ($\sigma_{13}$,$\sigma_{33}$) space.

With the specified material properties and geometry, the strength of this unit cell can be determined in pure shear, pure normal loading and in any combined loading.

Using Equations 2.3 and 2.5, the ratio of $(\sigma_{13}/\sigma_{33})$, 0.5, is equivalent to the numerical result shown in the failure surface of Figure 2.9. Also from Equations 2.3 and 2.5, the strength of the panel in pure tension and pure shear were analytically calculated to be 2.51 MPa and 0.52 MPa respectively, which is consistent with the strength result from the numerical calculations. The numerical model is the tool for analyzing complex failure mechanisms involving the interactions between multiple unit cells and the effects of strut failure in arrays of unit cells in truss core sandwich panels. The advantage of using the computational solutions is that the strength of arrays of multiple unit cells can be calculated; the redistribution of loads amongst the strut members is too complex to do in an analytically tractable manner. This approach also permits damage to be introduced into the array of unit cells, an advantage that is exploited and detailed in subsequent chapters.

# Chapter 3

# Experimental Validation of Analytical Predictions

## 3.1 Specimen Design and Fabrication

Truss core sandwich panels are usually fabricated from steel or aluminum alloys based on two approaches depending on the nature of the parent material used. One fabrication method was patented by Wallach and Gibson [20]. This involves folding a perforated metal sheet along node rows. Conventional joining methods such as brazing or laser welding are used to bond the core to the solid face sheets to form a sandwich structure. The folding of a perforated or expanded metal sheet provides a simple means to make lattice trusses. A variety of die stamping, laser or water jet cutting methods can be used to cut patterns into metal sheets. For example, a tetrahedral lattice truss can be made by folding a hexagonally perforated sheet in such a way that alternate nodes are displaced in and out of plane as shown to the right of Figure 3.1. By starting with a diamond perforation, a similar process can be used to make a pyramidal lattice as shown to the left of the figure. There is considerable waste material created during the perforation of the sheets and this contributes significantly to the cost of making cellular materials this way. These costs can be greatly reduced by the use of either clever folding techniques that more efficiently utilize the sheet material or methods for creating perforation patterns that do not result in material waste. Figure 3.1 to the left, also shows an example of the use of metal expansion techniques, followed by folding, that provides a means for creating lattice truss topologies with little or no waste. The entire process involved in making truss core panels by this method is detailed in Figure 3.1. The most widely

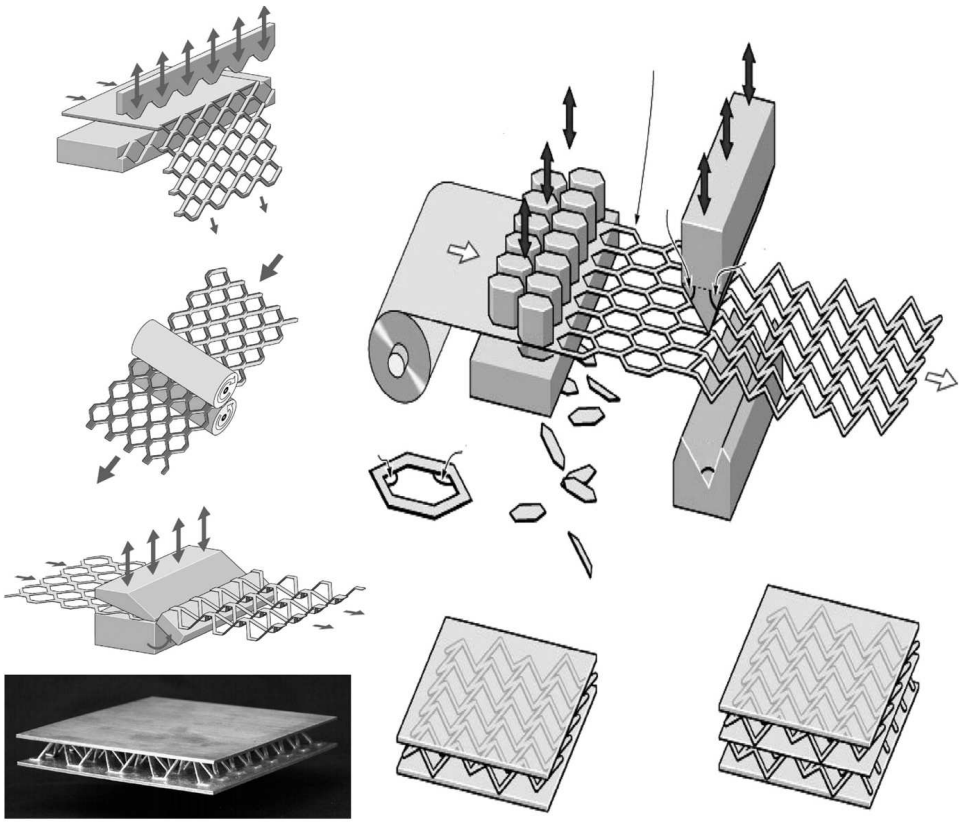

Figure 3.1: Figures adapted from Wallach and Gibson [20]. Left: A pyramidal lattice truss structure made by periodically slitting a metal sheet and then stretching (expanding) it. Alternate bending rows of nodes converts the expanded metal sheet into a pyramidal lattice truss structure. Right: A perforated metal sheet bent and bonded to create a tetrahedral lattice truss structure.

known drawback to this approach is the possible poor design of the core-face sheet node interface, as this ultimately dictates the maximum load that can be transferred from the face sheets to the core. When the node strength is compromised by poor joint design or inadequate bonding methods, node bond failure occurs, resulting in premature failure of the sandwich panel before the failure of the truss core structure [21]. However, the Wallach and Gibson approach took into consideration the numerous factors that could determine the robustness of the nodes, such as joint composition, microstructure, degree of porosity and the contact area. This approach has been proven to be more robust in fabricating an adequate joint [9]. The Wallach-Gibson approach is more suitable for sandwich structures made of steel material where laser welding can produce adequate node strength.

Another approach was proposed by Queheillalt et al [22], where an extrusion and electro-discharge machining (EDM) method has been developed to fabricate a pyramidal lattice core sandwich structure. In the approach as depicted in Figure 3.2, an aluminum alloy corrugated core sandwich panel is first extruded with integral core and face sheets. The corrugated core is then penetrated by an alternating pattern of triangular-shaped EDM electrodes normal to the extrusion direction to form the pyramidal lattice. The process results in a sandwich panel in which the core-face sheet nodes possess the parent alloy's metallurgical and mechanical properties. This method has been proven to be suitable for truss core sandwich panel made of aluminum alloys, as compared to core structure made of steel material, due to the difficulties involved in the extrusion of steel material. Another reason is that aluminum alloys are not good candidates for welding.

The specimens used for the experiments carried out in this research were fabricated using the Wallach-Gibson approach. Two pyramidal truss core sandwich panels were fabricated from stainless steel A 316L, one for testing in compression and the second for testing in shear.[1] For both tests, the panels were fabricated such that the geometry of the truss core are robust enough to undergo yielding before buckling; that is, $\sigma_{cr}$ is greater than $\sigma_y$. The buckling strength in the inelastic region is sufficient for comparing the experiment with the analytical prediction as the analytical critical strength ($\sigma_{cr}$) can be calculated using the Tangent or Reduced Modulus theory [23]. Table 3.1 details the parameters of the shear and compression specimens.

Table 3.1: Parameters of Shear and Compression Specimen

| | Shear Test Specimen | Compression Specimen |
|---|---|---|
| Face Sheet Thickness (mm) | 4.7 | 2 |
| Strut Length (mm) | 22 | 24.5 |
| Strut Cross-Sectional Area ($mm^2$) | 3.71 | 5.18 |
| Strut Inclination Angle (deg.) | 60.5 | 56.2 |
| Core Height (mm) | 19 | 20.5 |

[1]Specimens were manufactured by Cellular Materials International (CMI), Virginia, USA.

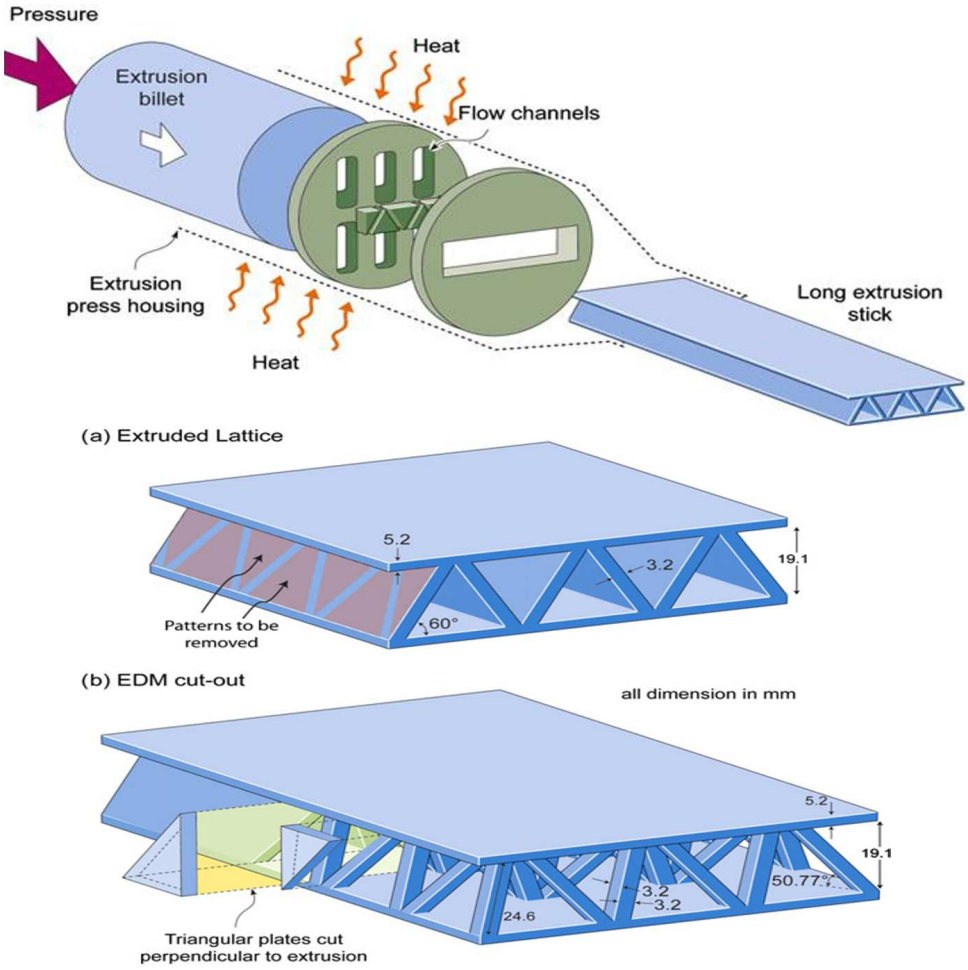


Figure 3.2: Schematic illustration of the extrusion process used to produce an aluminum alloy corrugated core followed by the schemes of the regions in the corrugated core that are removed by electrodischarge machining to create a pyramidal lattice core sandwich panel. Figures adapted from Queheillalt et al [22].

## 3.2 Experimental Procedure

To validate the predicted properties of the panel, compressive and shear test experiments were carried out on samples of pyramidal truss core panels. The truss structures were tested at ambient temperature at a displacement rate of $10^{-3}$ $\text{mms}^{-1}$ in accordance with ASTM C365 and C273 [24, 25] using compression platens and a shear rig respectively. Loading was applied through the Material Testing Systems (MTS) load frame machine, model 880, with 100 kN capacity. The shear rig was designed such that the loads applied through the load frame using the compression platens shear the truss core. A laser

extensometer (Electronic Instrument Research, EIR, Model LE-05) was used to measure the compressive strain by monitoring the displacements of the unconstrained face sheets while the shear strain was obtained by monitoring the displacements between the platens. A National Instruments Data Acquisition System was used to collect the incoming analog data from the laser extensometer. The system includes a SCC-2345 Signal Conditioner, 6251e DAQ PCI Card and a LabVIEW/DAQmx program created for data acquisition. Figure 3.3 shows the schematic illustration of the experiment equipment setup, with corresponding procedures of data acquisition and processing of the incoming data.

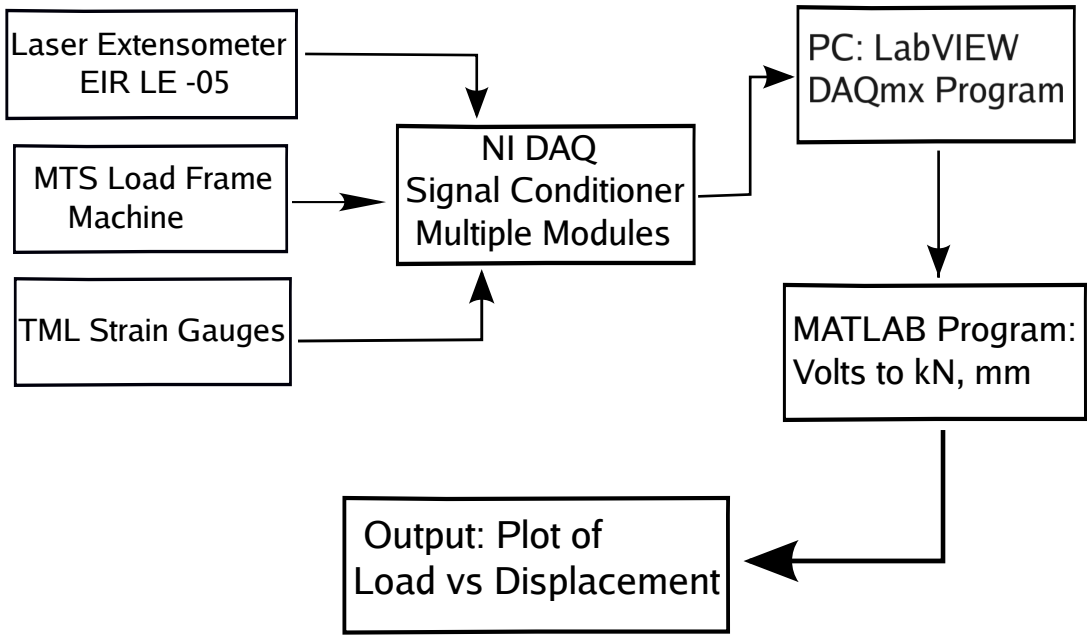


Figure 3.3: Schematic illustration of the experimental procedure showing the stages of data acquition and processing.

## 3.3 Variation in Strut Cross-Sectional Area

The effects of manufacturing flaws in the fabrication of the truss core panels used for the experiments were evaluated by the statistical method of Weibull distribution. By visual observation and measurement, it was evident that the thicknesses of the strut members vary from one another. As a result, in each experiment, the thickness of the strut to fail first (that is, the strut with the smallest cross-sectional area) varies. The Weibull analysis was used to provide accurate failure analysis and failure forecasts with extremely small samples [26]. The Weibull analysis was more suitable here because the number of

data samples available from the measurement of the struts' thicknesses were limited as only the struts on the outside of the panel could be reached for measurement. Another advantage of Weibull analysis is that it provides a simple and useful graphical plot of distribution data. The Weibull data plot is particularly informative as Weibull pointed out in 1951 [27]. The Weibull distribution usually provides the best fit of life data. This is due in part to the broad range of distribution shapes that are included in the Weibull family. Many other distributions are included in the Weibull family either exactly or approximately, including the normal, the exponential, the Rayleigh, and sometimes the Poisson and the Binomial. Even bad Weibull plots are usually informative to engineers trained to use them and the resulting Weibull analyses are still useful enough to provide valuable results. For extremely small samples of not more than twenty, the Weibull is the best choice, and therefore, best practice [26]. The requirement is to have most of the data samples around the fitted Weibull line, which in the case of the data samples measured from both the shear and compression specimens, more than 80% of the data samples show a good fit on the Weibull plot. For engineering evidence supporting another distribution, moderate size samples and large number of data are needed to discriminate between the Weibull and other distributions. Hence, Weibull analysis has become the most widely used in meeting engineering objectives in cases of extremely small samples.

Consequently, the Weibull distribution was utilized to describe the thickness distribution of the struts, in terms of their cross-sectional area. The goodness of fit of the strut data to a Weibull distribution was assessed by using a Weibull plot. The Weibull plot is a plot of the empirical cumulative distribution function, $\hat{F}(x)$, of data on special axes in a type of Q-Q plot [28]. The axes are $\ln(-\ln(1-\hat{F}(x)))$ versus $\ln(x)$. The variables for the axes were chosen such that the cumulative distribution function can be linearized in the form shown below;

$$\begin{aligned} F(x) &= 1 - e^{-(x/\lambda)^k} \\ -\ln(1-F(x)) &= (x/\lambda)^k \\ \underbrace{\ln(-\ln(1-F(x)))}_{\text{'y'}} &= \underbrace{k\ln x}_{\text{'mx'}} - \underbrace{k\ln\lambda}_{\text{'c'}} \end{aligned} \tag{3.1}$$

which can be seen to be in the standard form of a straight line. Therefore, if the data fit into a Weibull distribution then a straight line is expected on the Weibull plot. The Weibull parameters are the scale factor, $\lambda$, and the shape factor, k. There are a number

of approaches to obtaining the empirical distribution function [29] and in this case, the MATLAB Weibull plot function was used. From the linear regression used to numerically assess the goodness of fit, the two parameters of the Weibull distribution can be estimated. The gradient informs one directly about the shape parameter k. The scale parameter $\lambda$ can be obtained from the y-axis: $\ln(-\ln(1-\hat{F}(x))) = 63.2\%$ ordinate point. The shape and scale parameters were calculated with the MATLAB Weibull function. For the case of the truss core panel, it means that if $\lambda$ is the characteristic dimension of the struts, this would be the area at which 63.2% of the struts will fall below the expected area, with the mean being the expected area of the struts. For the compression specimen, the thicknesses of 23 struts were measured and their cross-sectional area calculated, while it was possible to reach and measure the thicknesses of 42 struts from the shear specimen. The Weibull plot on the distribution of the area was evaluated with Equation 3.1 with the calculations carried out using MATLAB Weibull plot function. The distributions show a good fit as shown in Figures 3.4 and 3.5 for the compression and shear specimens respectively.

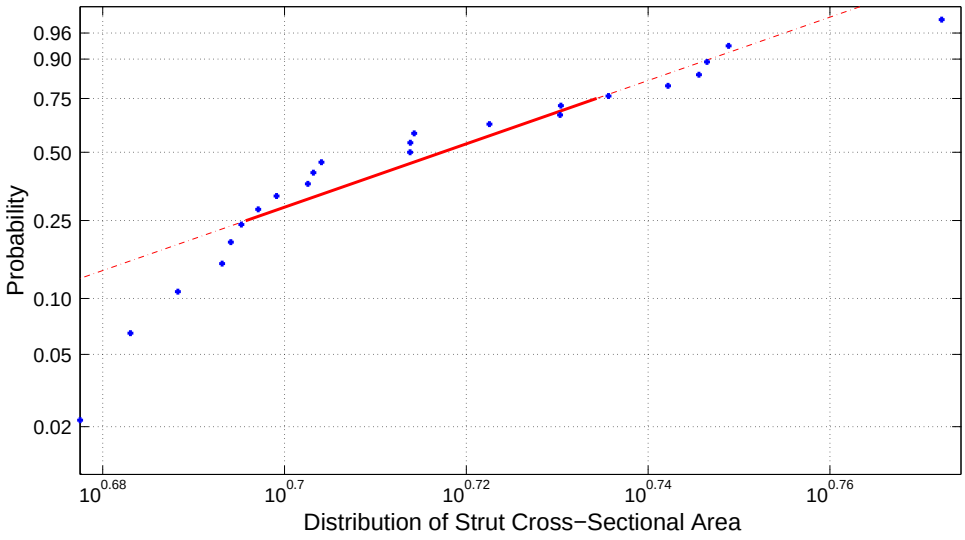


Figure 3.4: Weibull goodness of fit check on the struts of the compression specimen using the measured cross-sectional area of 23 struts.

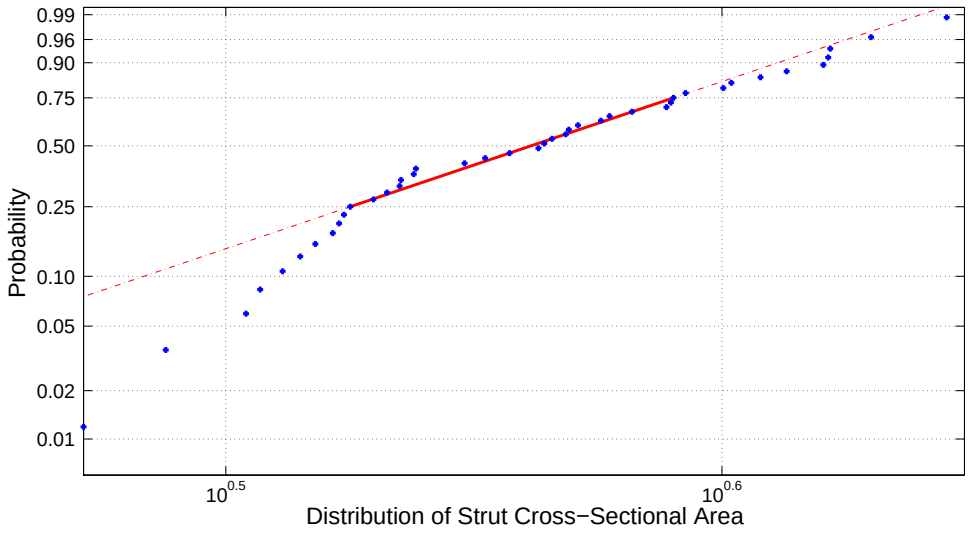


Figure 3.5: Weibull goodness of fit check on the struts of the shear specimen using the measured cross-sectional area of 42 struts.

The distributions from the compression specimen gave an estimated mean strut cross-sectional area of 5.18 mm$^2$, a standard deviation of 0.14 mm$^2$, and Weibull shape and scale parameters of 17.15 and 5.35 mm$^2$ respectively. The struts of the shear specimen have an estimated mean cross-sectional area of 3.71 mm$^2$, standard deviation of 0.121 mm$^2$, and Weibull shape and scale parameters of 12.98 and 3.86 mm$^2$ respectively. The distributions of the probability density are shown in Figures 3.6 and 3.7 for the compression and shear specimens respectively, and this may also be calculated such that the integral over all the bounded struts area take the value of unity.

The compressive test sample has a face sheet thickness of 2 mm, strut (mean) cross-sectional area, $\bar{A}_{cp}$, of 5.18 mm$^2$ from the Weibull analysis, a core height of 20.5 mm, strut length of 24.5 mm and a strut inclination angle of 56.2°. While the relative density, $\bar{\rho}_{cp}$, of the truss core was calculated as below:

$$\bar{\rho}_{cp} = 0.067 \tag{3.2}$$

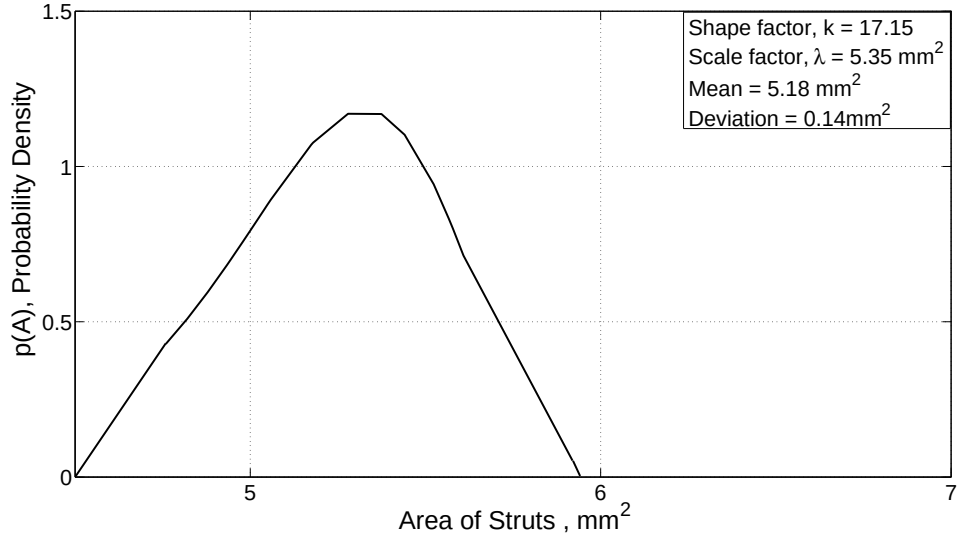


Figure 3.6: Weibull probability density against the cross-sectional area distribution in the 23 struts of the Compression Specimen.

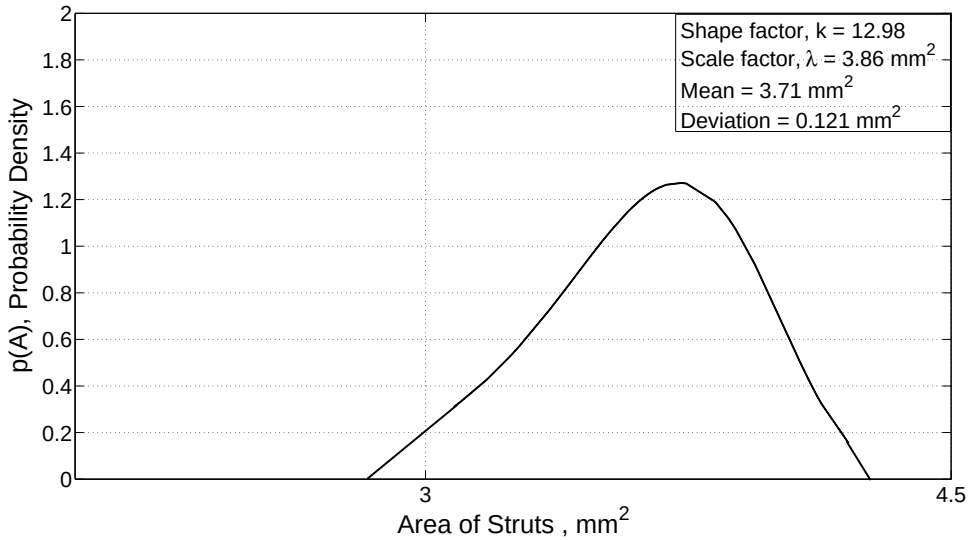


Figure 3.7: Weibull probability density against the cross-sectional area distribution in the 42 struts of the Shear Specimen.

The specimen fabricated for the shear experiment was made of thick face sheet but with rather slender truss elements, to ensure that the shearing of the panel is solely carried by the struts, while the struts are still sufficiently robust and strong enough to undergo yielding before buckling. The shear test specimen has a mean cross-sectional area ($\bar{A}_{sh}$) of 3.71 mm$^2$ from the Weibull analysis, web thickness of 1.9 mm, a core height

of 19 mm, strut length of 22 mm and a strut inclination angle of 60.5°. The relative density, $\bar{\rho}_{sh}$, of the shear truss core sample was calculated as below:

$$\bar{\rho}_{sh} = 0.069 \tag{3.3}$$

## 3.4 Compression Experiment

Before the compression tests were carried out, tensile coupons of the stainless steel parent material cut out from the panel face sheet were tested to determine the mechanical properties of the parent steel material. This test was carried out to determine the material properties of the fabricated truss core structure, which could have changed from the initial material properties of the 316L stainless steel used, due to the effects of welding, annealing and other fabrication processes. Tensile tests were performed according to ASTM E8 at a displacement rate of $10^{-3}$ $\text{mms}^{-1}$ on three samples. The average Young's modulus, $E_s$, and 0.2% offset yield strength, were 197.6 GPa and 283 MPa, respectively. Figure 3.8 shows the stress-strain response from one of the tested samples.

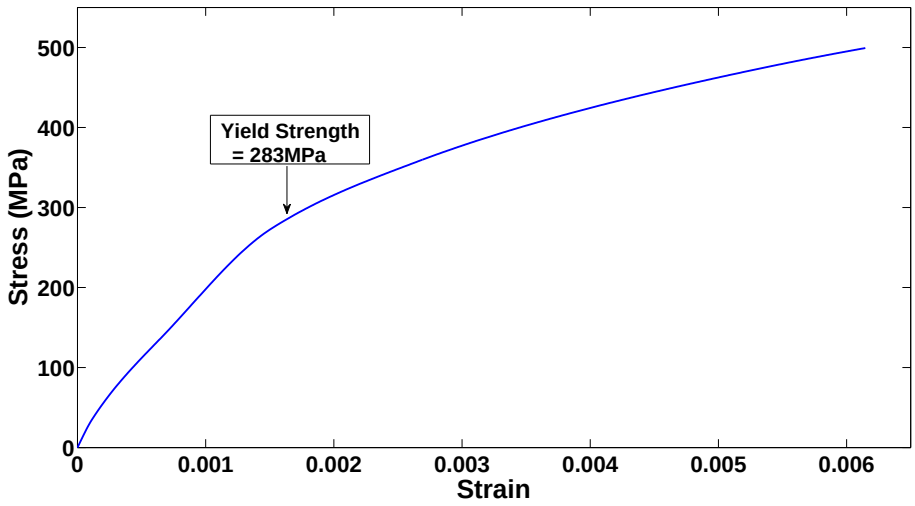


Figure 3.8: Stress–strain curve of the sandwich panel parent material, under simple tensile test.

The specimens were cut into 2X2 unit cell samples with all the nodes fully intact and

protected during the cutting and milling operation. The face sheets of the compression specimens were ground to improve the parallelism between the face sheets, to reduce the effect of uneven load distribution in the unit cells. The 2X2 unit cell sample was placed between the compression platens of the load frame such that the entire face sheets were in full contact with the platens, while the laser extensometer sensor tape was attached on the edges of the face sheets. The sample was loaded at a nominal displacement rate of $10^{-3}$ $\text{mms}^{-1}$ in accordance with ASTM C365. Two sets of tests with identical specimens were performed under the same conditions, and the results from both test show approximately the same value within a difference of 5%. The compressive stress-strain response of truss core panel is shown in Figure 3.9 while Figure 3.10 shows the pictures of the panel at different strain levels. Following an initial linear response, plastic yielding of the truss core occurred and a peak was then observed in the compressive stress that coincided with initiation of the buckling of the truss members, along with the formation of plastic hinge near the mid-sections of the members. Continued loading resulted in core softening, at which point the load increased rapidly as the deformed trusses made contact with the face sheets. Figure 3.11 shows the compressive stress to strain response of the compression specimen. The measured compressive strength was compared to the predicted strength of the panel to assess the accuracy of the prediction.

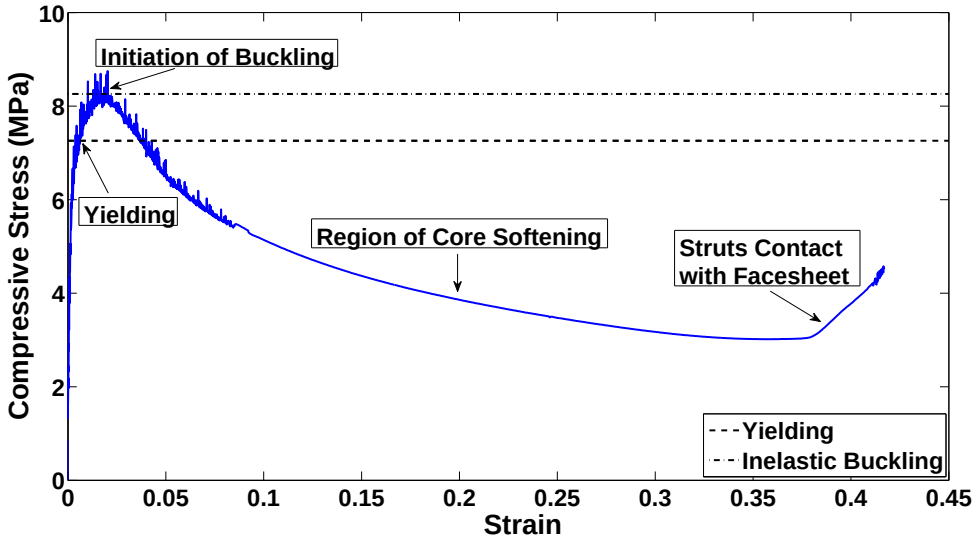


Figure 3.9: Measured yielding and inelastic buckling in a full graph of the compressive stress vs. strain response of a typical truss core panel.

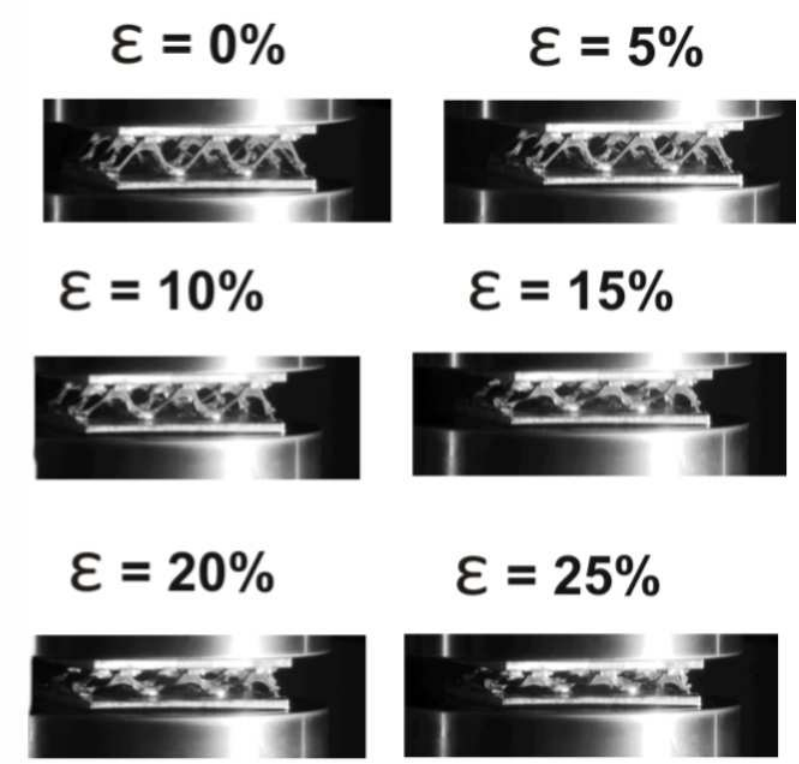


Figure 3.10: Photographs of the pyramidal truss core sandwich panel deformation at different strain levels.

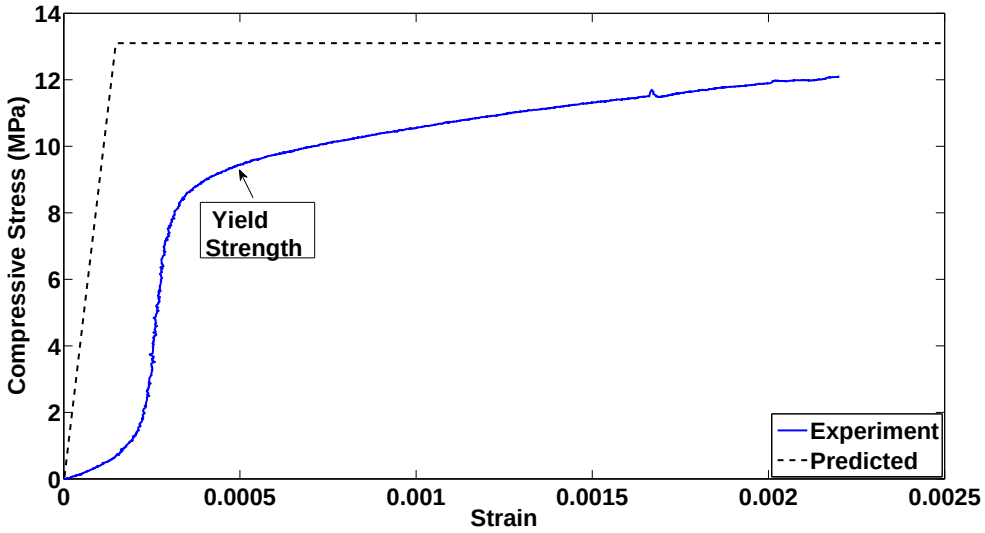


Figure 3.11: Compressive stress vs. strain response of the pyramidal truss core panel, for the compression specimen provided by CMI. Comparison of experimental measured strength with the predicted strength.

## 3.5 Shear Experiment

For the shear tests, a shear rig was designed such that the panel is loaded in shear by a force applied through one edge of the face sheet, while the other face sheet is constrained at the other edge. The direct shear experiment was carried out on arrays of unit cells as shown in Figure 3.12. The loaded and constrained edges were ground and machine milled to ensure they sit flat on the surface of the shear rig at the surface of contact. The specimens were cut into 2.5X2.5 unit cell samples with all the nodes fully intact. As shown in Figure 3.13, a clamping device was used to support the sample in the shear rig to resist rotation of the specimen due to the net moment exerted by the test fixture, while the entire top and bottom surfaces of the shear rig were fully in contact with the platens.

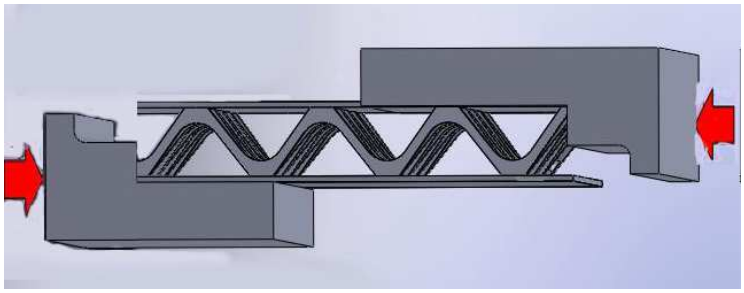

Figure 3.12: Direct shear test as carried out on the sandwich panel sample.

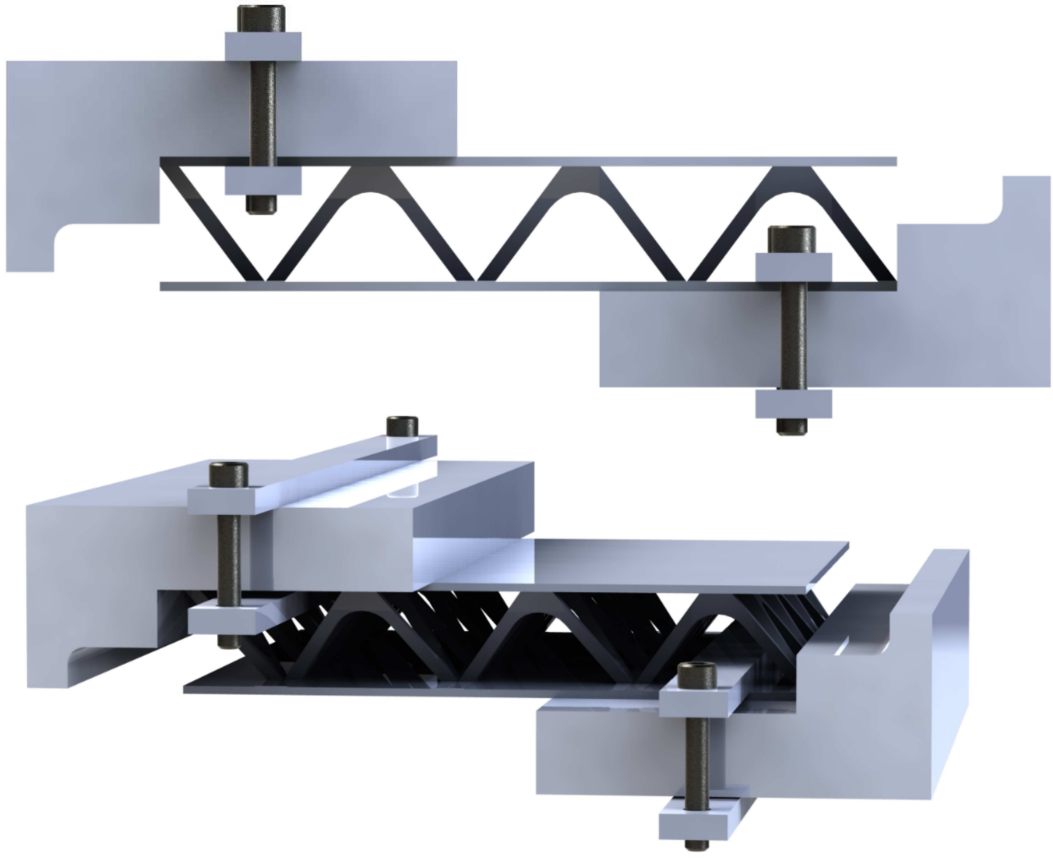

Figure 3.13: The shear test specimen showing the clamping of the specimen to resist rotation caused by the net moment.

Laser sensor tapes were attached on the platens and a laser extensometer recorded the displacements. The test samples were loaded at a nominal displacement rate of $10^{-3}$ $\text{mms}^{-1}$ in accordance with ASTM C273. Two sets of test were first performed with the samples under the same conditions, for comparisons of the results to ensure consistency. In the test orientation as shown in Figure 3.14, each unit cell had two truss members loaded in compression and the other two in tension. The test sample exhibited the expected characteristics under a shear test (with the struts subjected to loading in tension and compression), while yielding occurred before buckling. Figure 3.15 shows the shear stress to strain response of the panel.

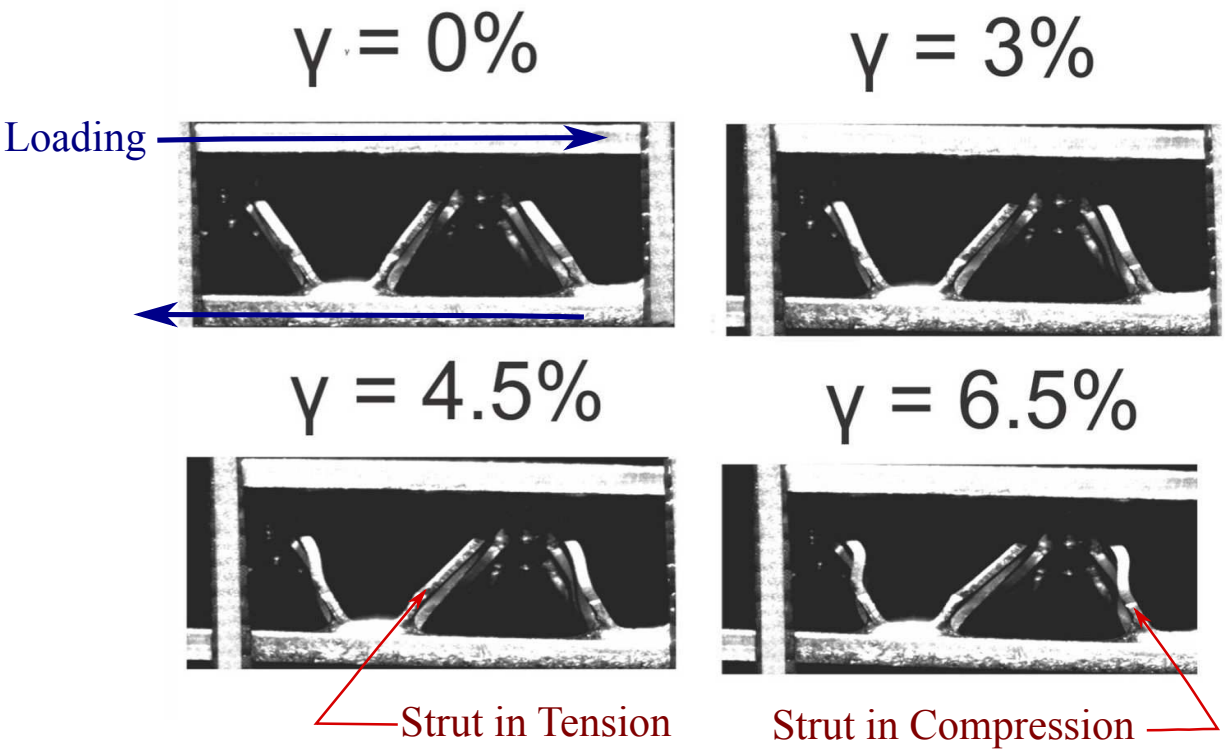


Figure 3.14: Struts of the pyramidal truss core panel in compression and tension under the applied shear.

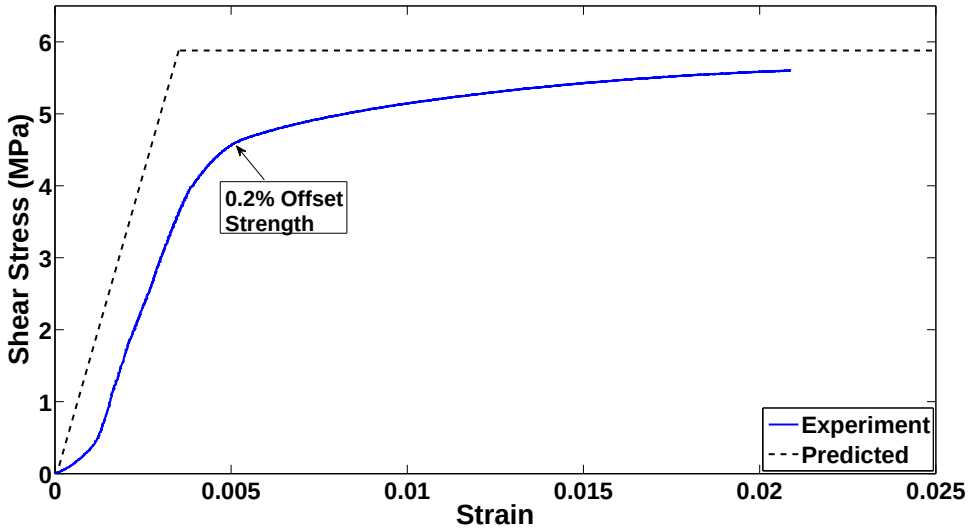


Figure 3.15: Shear stress vs. strain response of the pyramidal truss core panel, for the shear specimen provided by CMI. Comparison of experimental measured strength with the predicted strength.

## 3.6 Result Comparisons

From the compressive stress-strain response shown in Figure 3.11, an initial high-compliance region was caused by concavity of the panel face sheets induced during machining. The expected linear elastic region follows with a stiffness of 3.78 GPa, which is 1.6% less than the predicted stiffness. The stiffness of the panel was measured at the region of the steepest slope along the linear elastic region of the stress-strain plot. The failure strength of the panel was taken to be equivalent to the yield strength observed at obvious yield point where the stress-strain plot becomes non-linear or at 0.2% offset strain if there is no clear non-linear region, and this value was directly compared to the predicted strength. A compressive strength ($\sigma_{33exp.}$) of 9.73 MPa was measured at the obvious yield point as shown in Figure 3.11. The strength at 0.2% offset strain was used for the shear test and a strength ($\sigma_{13exp.}$) of 4.72 MPa was measured.

The predicted compressive strength ($\sigma_{33pred.}$) of the specimen calculated from the Weibull analysis in Equation 3.2 and by substituting that into Equation 2.3 gives:

$$\sigma_{33} = 13.1 \text{ MPa}. \tag{3.4}$$

The predicted shear strength ($\sigma_{13pred.}$) of the specimen for the shear tests follows by substituting $\bar{\rho}_{sh}$ (calculated from the Weibull analysis) into Equations 2.5, which results into;

$$\sigma_{13} = 5.92 \text{ MPa}. \tag{3.5}$$

For the geometry of the truss core sandwich panels used in these experiments, the predicted non-dimensional compressive strength of the panel in terms of the ratio of ($\sigma_{33}/\sigma_y$) is 0.046, while the predicted non-dimensional shear strength of the panel is 0.021. Based on the normalized stress space, the predicted strength is equivalent to the unit factor of 1 as shown in the normalized axes of Figure 2.6. A normalized compressive strength of 0.76 was measured, which was 24% less than the predicted compressive strength. In the same manner, a normalized measured shear strength of 0.80 was calculated from the experiment, which was 20% less than the predicted strength. One reason for these discrepancies is lack of perfect parallelism of the face sheets; some of the struts were more highly loaded than others. In addition, because of small irregularities in the manufacturing process, the unit cells were not perfectly identical. These factors contributed to

the differences recorded in the experimental results when compared to the analytical and numerical predictions.

# Chapter 4

# Predicting Damage and Residual Strength

## 4.1 Mimicking Damage–Numerical Analysis

In the previous chapter, the strength of pyramidal truss core panel was investigated in the undamaged state and the experimental validation of the predictions discussed. However, the panel will undergo damage under continuous mechanical loading during use, due to fatigue, corrosion and impact loading. It is therefore important to understand how the strength of the panel degrades when damaged and the residual strength of the panel in the damaged state. For this purpose, numerical calculations of the behavior of a 2X2 unit cell specimen subjected to combined loading along the $X_2$ and $X_3$ axes under a set of symmetrical minimum boundary conditions were performed. The sets of boundary conditions were chosen such that the panel is not unnecessarily over-constrained for the purpose of the numerical calculations. As shown in Figure 4.1, the chosen boundary conditions also ensure symmetrical load distribution along the $X_1$ and $X_2$ loading direction, keeping to the symmetry of the panel. With the ratio of applied shear to applied compression held constant, damage was inflicted on the panel by loading the undamaged panel until a strut member failed in either yielding or buckling. The failed strut member was removed and the macroscopic strength of the resulting panel calculated while keeping the same ratio of shear to compression. The next strut that failed was then removed (simulating the case of a panel with two struts damaged). The strength of the resulting panel is then calculated, and the subsequent strut to fail is removed, thus representing the case of a panel with three struts damaged. Figures 4.1 and 4.2 show the trend of damage

propagation for the case of pure shear and pure compression respectively. By following this procedure of damage analysis, the residual mechanical strength of damaged truss core panel can be determined through numerical calculations and the resulting failure surfaces of the damaged panel can be obtained.

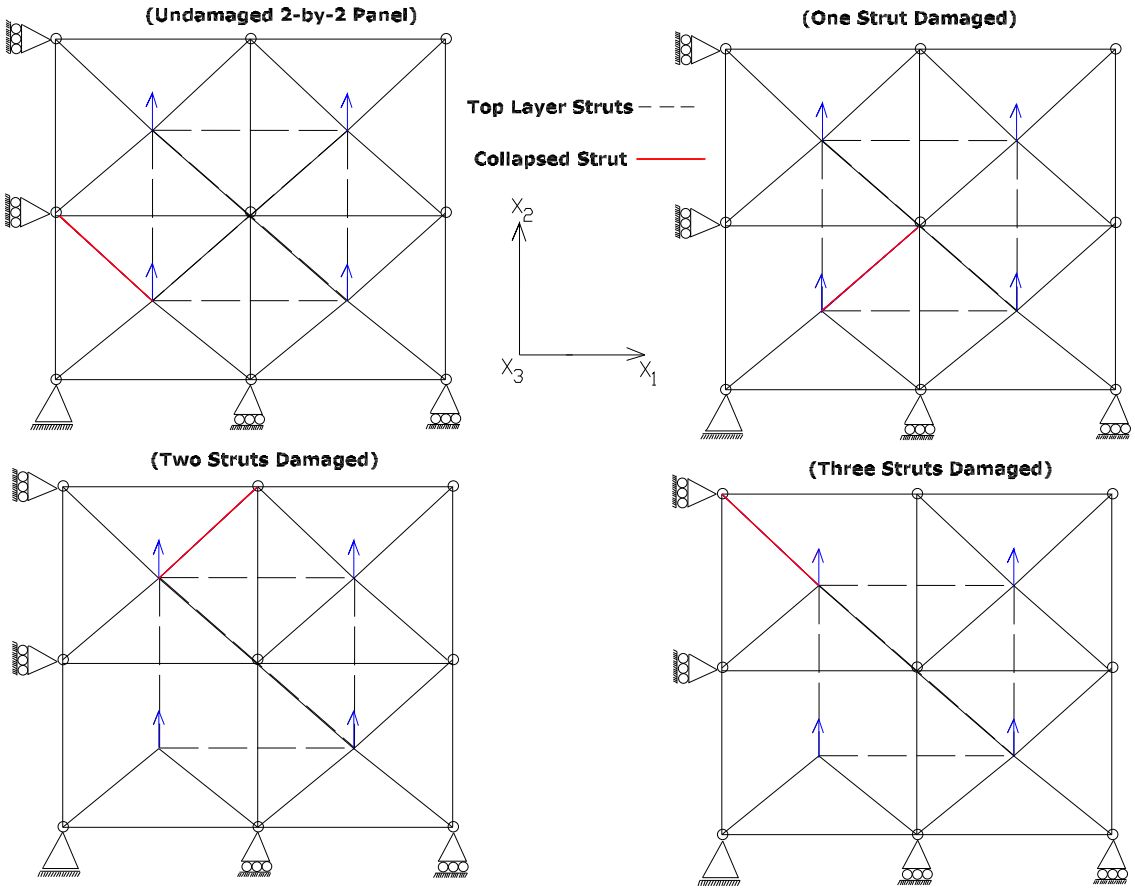


Figure 4.1: Damage trend in pure shear. Top view of the 2X2 unit pyramidal truss core panel. The dashed lines denote the squared lattice of the top layer while the regular lines represent the squared bottom layer with the four diagonal lines in each unit cell representing the pyramidal core. The damaged strut is shown in red and the direction of loading shown by the blue arrows. The boundary conditions are shown by the supports and all bottom nodes constrained in the $X_3$ direction.

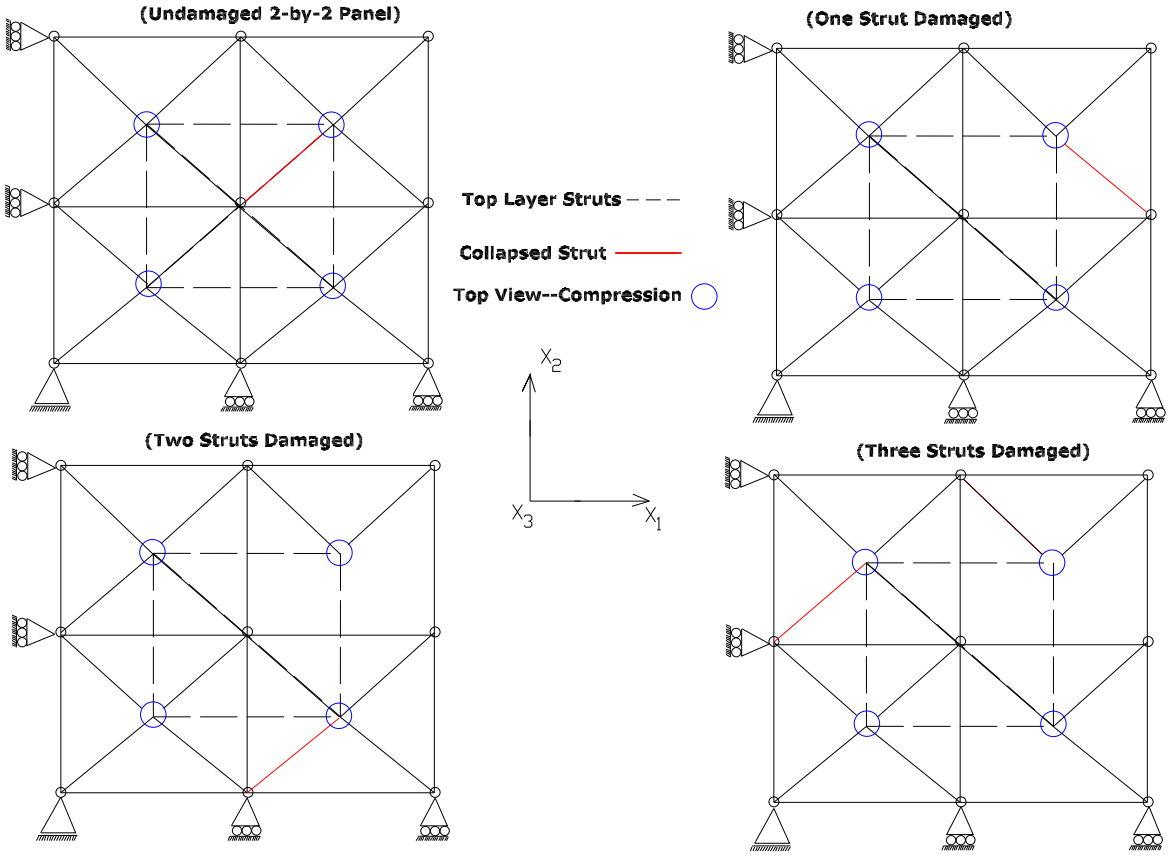


Figure 4.2: Damage trend in pure compression. Top view of the 2X2 unit pyramidal truss core panel. The dashed lines denote the squared lattice of the top layer while the regular lines represent the squared bottom layer with the four diagonal lines in each unit cell representing the pyramidal core. The damaged strut is shown in red and the compression load shown by the blue circles. The boundary conditions are shown by the supports and all bottom nodes constrained in the $X_3$ direction.

## 4.2 Numerical Calculation of Damaged State Strength

The rate at which the macroscopic strength of the panel degrades is related to the amount of damage the panel suffers. For the examination of damaged state strength, a 2X2 unit cell panel was simulated under combined loading with the symmetrical boundary conditions described in Section 4.1. Under each ratio of applied shear to applied compression considered, damage was inflicted on the panel from the undamaged state up to three struts damage, and the numerical calculations give the failure surfaces, shown in Fig-

ure 4.3. The pyramidal core used for the damaged state numerical analysis has strut length of 27.5 mm, radius of 0.69 mm, angle made by struts with face sheet ($\omega$) of 55°, Young's modulus $E$ of 69 GPa and yield strength $\sigma_y$ of 255 MPa, similar to the geometry of the panel used in Section 2.3, which was a single unit cell. It should be noted that a pyramidal core with struts having rectangular cross-sections could also be used for this analysis since the required parameters from the core geometry are the strut area and the relative density. Table 4.2 shows the percentage degradation of the panel overall strength owing to damage in pure shear and pure compression. The numerical calculations of the failure surfaces follow the procedures of mimicking damage as discussed in Section 4.1. In each damaged state, displacements were applied on the apex nodes of the panel and the resulting stresses in the strut members calculated to determine the failing struts in order to compare the predicted strength degradation of the panel in pure shear and compression with the measured strength.

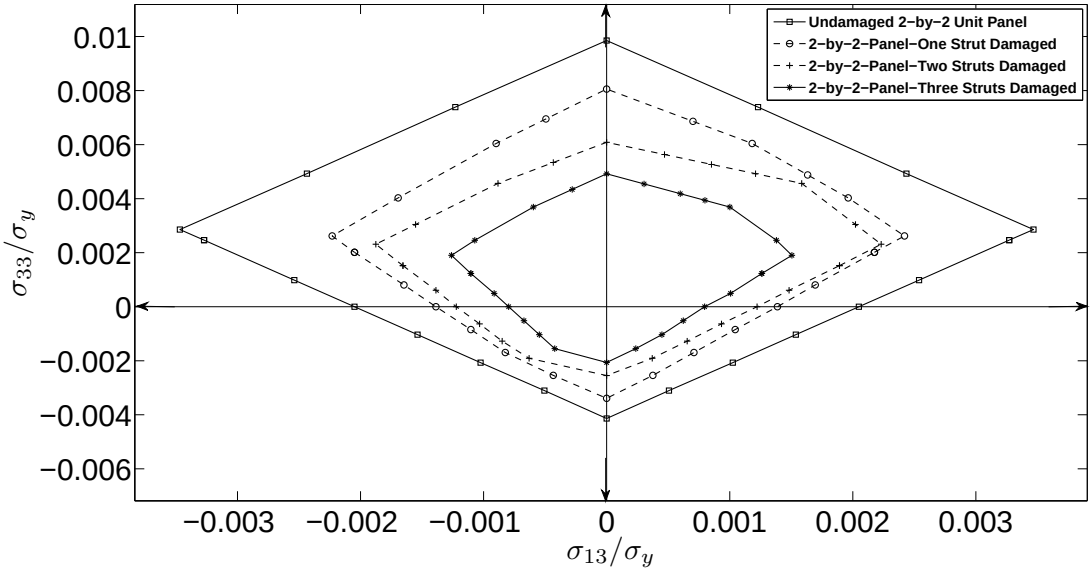


Figure 4.3: Failure surfaces showing the strength of the 2X2 unit pyramidal panel in the damaged state. Damage inflicted up to three struts.

Table 4.1: Damage Degradation of Strength, Minimum BC

| | Shear Strength, MPa | % Shear Strength | Compressive Strength, MPa | % Compressive Strength |
|---|---|---|---|---|
| Undamaged | 0.51 | | 1.05 | |
| One-Strut Damaged | 0.36 | 72 | 0.86 | 82 |
| Two-Strut Damaged | 0.31 | 61 | 0.65 | 62 |
| Three-Strut Damaged | 0.22 | 43 | 0.53 | 50.5 |

## 4.3 Damaged State Experimental Comparison

### 4.3.1 Damaged State Compression Experiment

Compression tests were carried out on damaged samples of pyramidal truss core to compare the predicted damaged strength to experiments. This provides more insight into the actual behavior of the panel and demonstrates if the numerical approach is accurate. The test preparation and setup are identical to the procedures detailed in Section 3.4. The test specimens have the same geometry and material properties as the specimens in Section 3.4. One of the goals of the damaged state experiment is to capture the mechanical response of a few selected struts during the test. The aim was to compare the strains in the struts measured during the experiments to the predicted strains of same struts calculated numerically. The strains in the struts were captured by the same data acquisition system described in Section 3.2, with strain gauges attached on the selected struts. Strain gauges used were of 1 mm gauge length with a gauge factor of 2.14 and gauge resistance of 120 ohms. The strains in the struts were calculated from the measured strain as below;

$$V_\epsilon = \frac{V_O' - V_O}{V_{EX}}, \tag{4.1}$$

where $V_O'$ is the measured output voltage when strained, and $V_O$ is the initial, unstrained output voltage. $V_{EX}$ is the excitation voltage. Also, the designation $(+\epsilon)$ and $(\epsilon)$ indicates active strain gauges mounted in tension and compression, respectively. For the quarter bridge connection as used in the experiments, the strain in the struts is calculated as a function of the $V_\epsilon$ as shown below:

$$\epsilon = \frac{\pm 4V_\epsilon}{GF(1+2V_\epsilon)}(1+\frac{R_L}{R_G}), \tag{4.2}$$

where $R_L$ is the lead resistance, $R_G$ is the gauge resistance, and $GF$ the guage factor of the strain gauge.

Before damage was inflicted on the panel, an undamaged sample was tested to identify which strut to damage first. In the numerical calculation for the undamaged state, the struts are equally stressed as the geometry is perfectly modeled and there is even load distribution in the unit cells which are connected by truss elements representing the face sheets. But this will not be the actual behavior of the specimen owing to the presence of manufacturing imperfections and the interactions between the unit cells in the way they are joined to the face sheets. For these reasons, three sets of struts were identified based on the expected mechanism governing the response of the struts under normal loading. Figure 4.4 shows the representation of the three sets of struts. It was expected that the struts in each set would have approximately the same mechanical response to normal loading. Set $I$ represents the innermost struts in the 2X2 unit cell panel, Set $II$ represents the struts lying in-between the innermost the outermost struts, while Set $III$ represents the outermost struts.

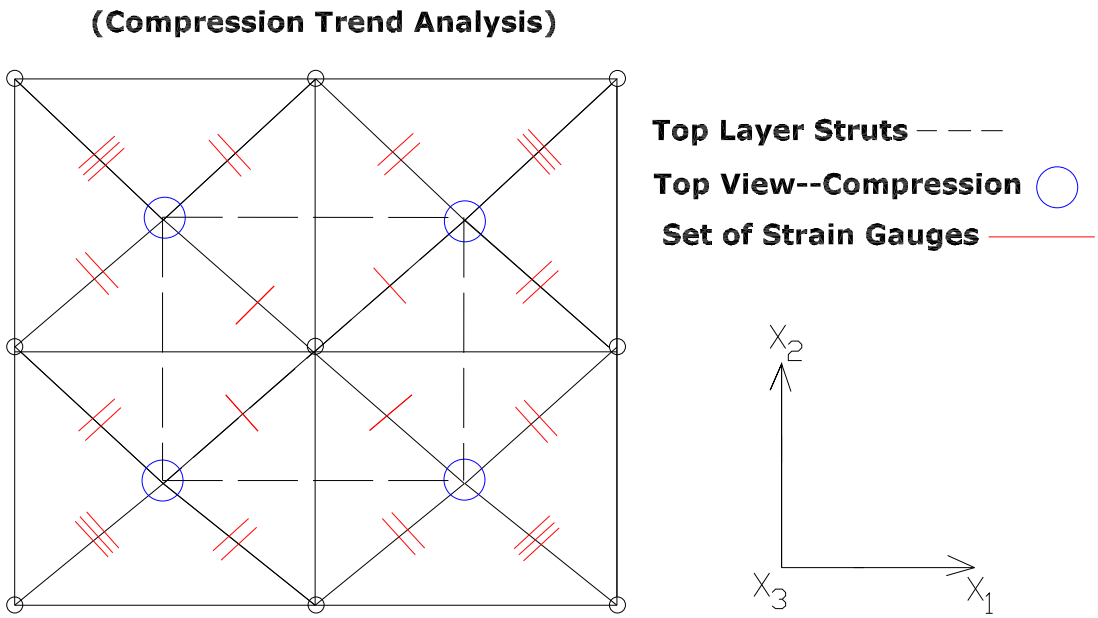


Figure 4.4: Undamaged 2X2 unit pyramidal panel showing the three sets of struts to which three strain gauges were attached. A strain gauge was attached on a strut from each set.

Two tests were carried out and in each test, a strain gauge was attached on a strut each from the sets $I$, $II$, and $III$. For the two tests, different struts were chosen from each of the sets $I$, $II$, and $III$. Figure 4.5 shows the layout of one of the undamaged state test carried out, while the macroscopic load-displacement response of the panel is shown in Figure 4.6. For the macroscopic strength, the displacements between the face sheets were captured by the laser extensometer as detailed in Section 3.2. The failure strength of the panel was taken at the region where a clear yield point (non-linear region) is seen in the plotted load-displacement graph. For cases where the yield region was not obvious, the stress at 0.2% offset strain was chosen. The stiffness of the panel was measured at the region of the steepest slope along the linear elastic region of the load-displacement plot. Although there is a long plateau in strength which corresponds to the peak strength of the panel prior to buckling, the clear yield point or the 0.2% offset strength were chosen as they are more accurate measure of the core strength at plastic yield. This was the value directly compared to the numerical strength predictions. Figures 4.7 and 4.8 show the corresponding applied load to strain response of the struts. The strains measured in the struts are non-linear due to bending and buckling of the strut, which result in the

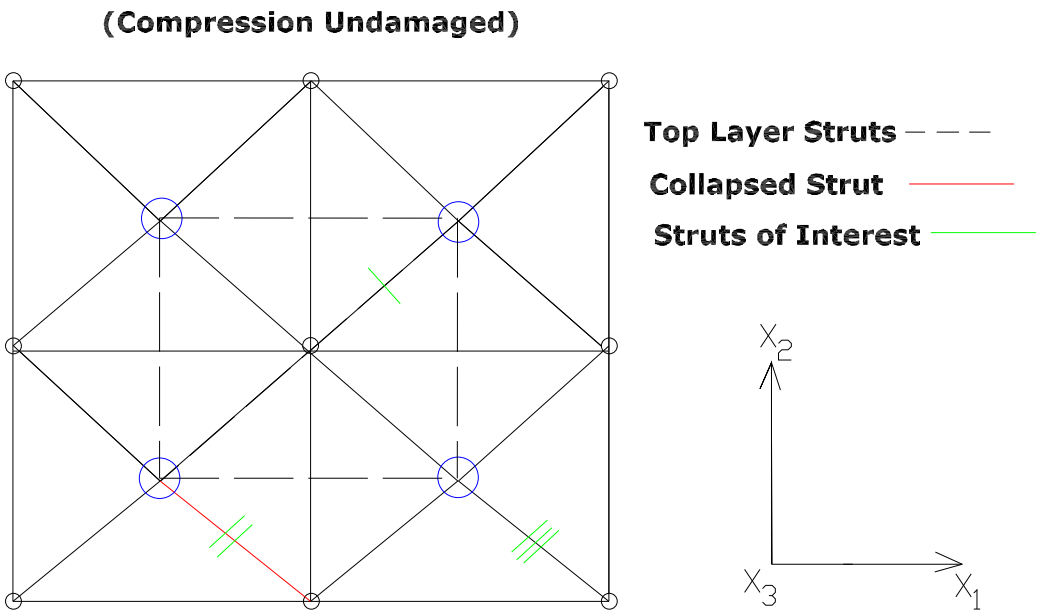


Figure 4.5: Undamaged 2X2 panel loaded in compression. The Roman numerics denote the three struts of interest. The failing strut is shown in red while the blue circles denote the loading in compression.

tension of the convex side. From the results of these two tests, the experimental results indicate that the struts in set $II$ experience higher strain than the struts in set $I$ and $III$. However, there was no consistency in the strain response from the struts of same set between the two tests. Therefore, the results from these two tests are not conclusive. The differences can be attributed to the manufacturing flaws in the specimens, having shown in Section 3.3 the varying thicknesses of the struts, which is close to about 12% for the compression specimens. Another factor is that imperfect struts bend in compression. During one of the tests, two strain gauges were attached on the opposite sides of a strut to determine if the strut bends. It was found that the strut experiences bending during the test.

Owing to the results from the two tests carried out, one of the struts from set $II$ was damaged. From the macroscopic load-displacement response of the 2X2 unit panel in the undamaged state, the measured failure load was 16.4 kN, which gave a strength difference of 16% when compared to the predicted load of 19.5 kN. The measured stiffness of the panel was 3.79 GPa, which gave a difference of 1.3% when compared to the predicted stiffness of 3.84 GPa.

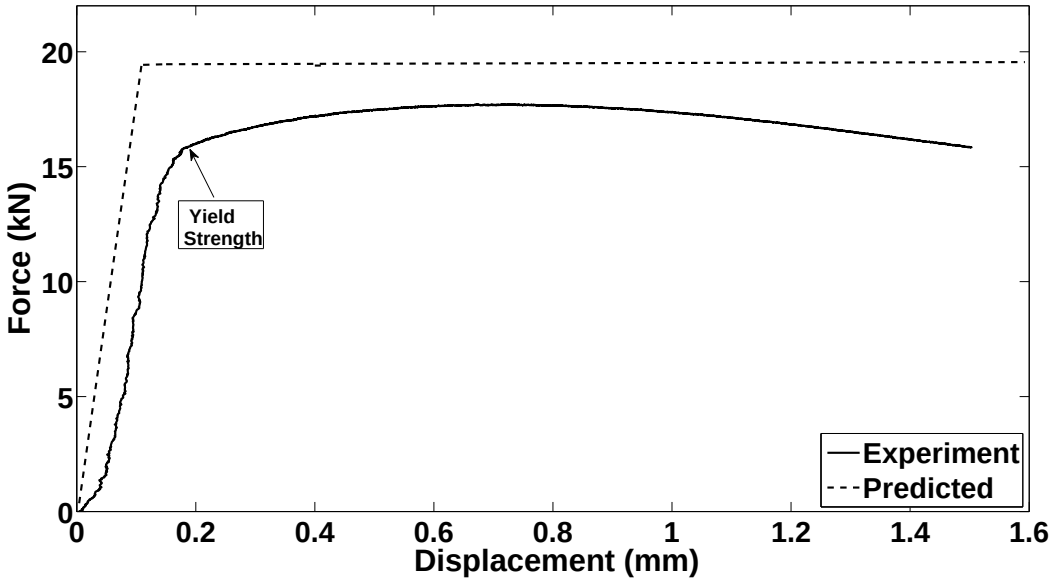


Figure 4.6: Load vs. Displacement graph of undamaged 2X2 pyramidal truss core panel, specimen loaded in compression. Comparison of measured strength with predicted strength.

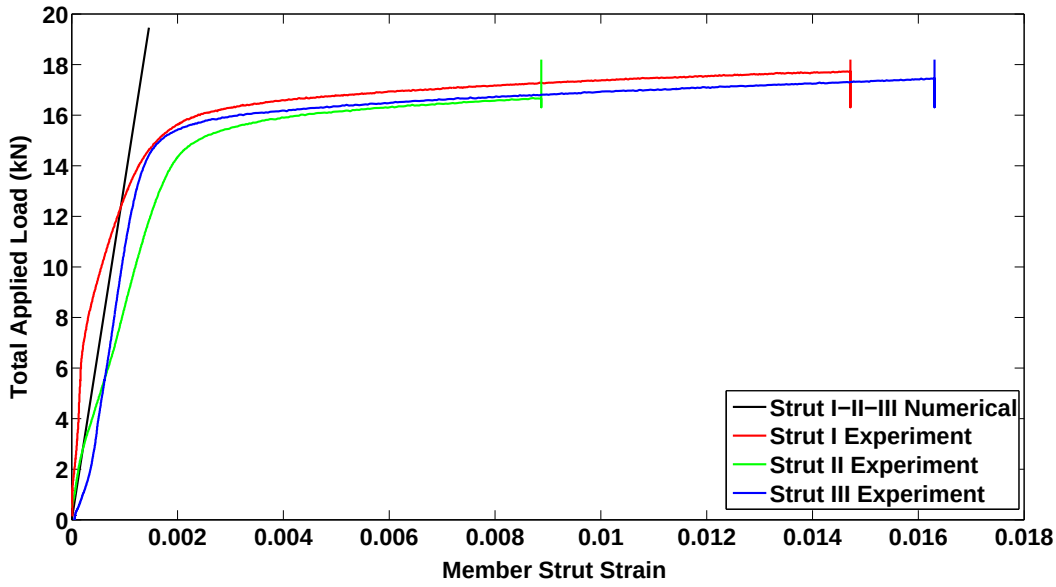


Figure 4.7: Experiment-Numerical comparison of the strains in the selected struts of the undamaged 2X2 pyramidal truss core panel. Graph of applied load against the strain in the members. Specimen loaded in compression.

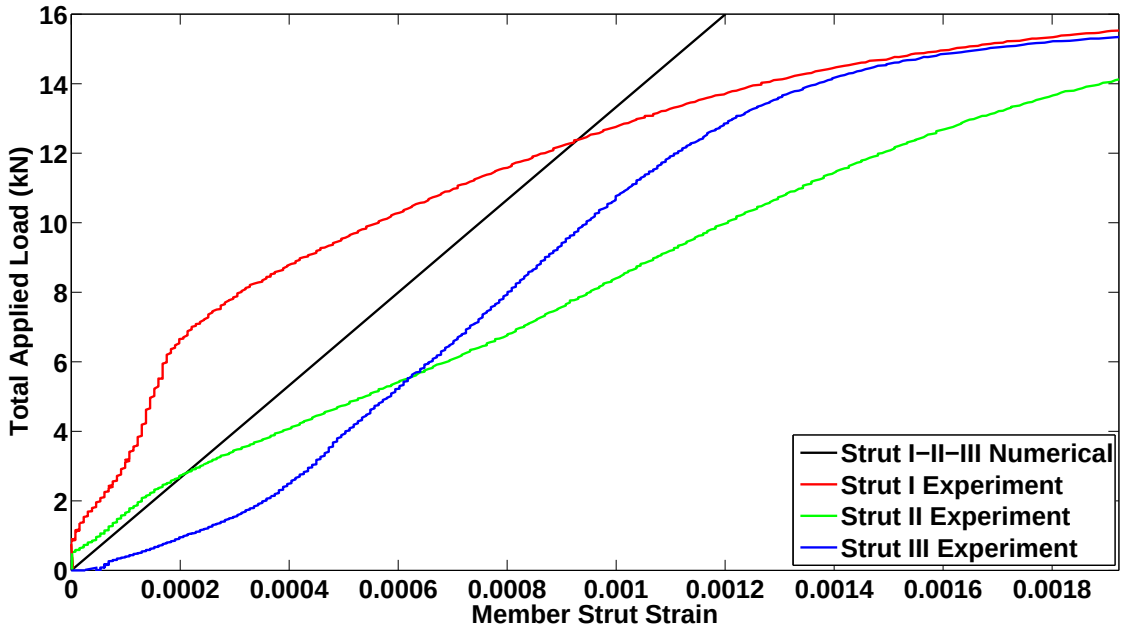


Figure 4.8: Experiment-Numerical comparison of the strains in the selected struts of the undamaged 2X2 pyramidal truss core panel. Graph of applied compressive load against the strain in the members, magnified plot for clarity in comparisons.

For the one-strut damaged test, the damaged strut from Set $II$ of the undamaged state is shown missing in Figure 4.9 and the selected three struts of interest are marked in the order of stresses in them with struts $I$ and $III$ expected to be experiencing the maximum load at failure followed by strut $II$. Figure 4.9 test configuration was meant to compare the numerical predictions of the behavior of struts $I$ and $III$ which are expected to be having approximately the same magnitude of stresses at failure, and are predicted to be more than the stress level in strut $II$. An important result from this test is the comparison between the measured macroscopic strength of the damaged panel and the numerical prediction. Figure 4.10 shows the load-displacements plot corresponding to this. The measured failure load was 12.41 kN, which gave a strength difference of 19.5% when compared to the predicted failure load of 15.6 kN. The measured stiffness of the panel was 3.64 GPa, which gave a difference of 8.7% when compared to the predicted stiffness of 3.97 GPa. Figures 4.11 and 4.12 shows the corresponding applied load to strain response of the selected struts of interest. The strains are consistent with the numerical prediction according to the rank order of the stresses (or strains) in the struts.

As mentioned earlier, the strains in the struts are not equal in magnitude owing to the effect of bending in the compressed strut. The varying thicknesses of the struts is another factor contributing to this. However, the rank oder of the strain level measured in the struts is consistent with prediction and this validates the predicted trend of damage propagation because it follows a similar pattern as the numerical analysis. The next damaged state experiment was performed with strut *III* damaged.

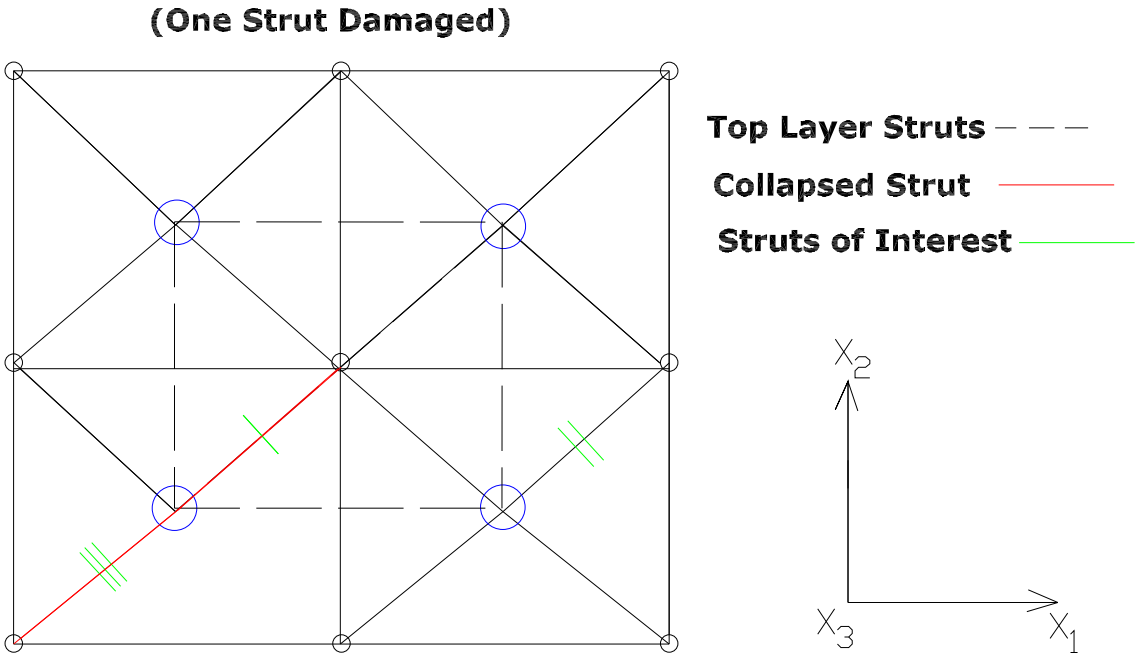


Figure 4.9: One-strut damaged 2X2 panel loaded in compression. Damaged strut shown as the missing strut in the bottom-left cell and the Roman numerics denote the three struts of interest. The predicted failing struts are shown in red while the blue circles denote the loading in compression. Struts I and III were predicted to have same stresses at failure.

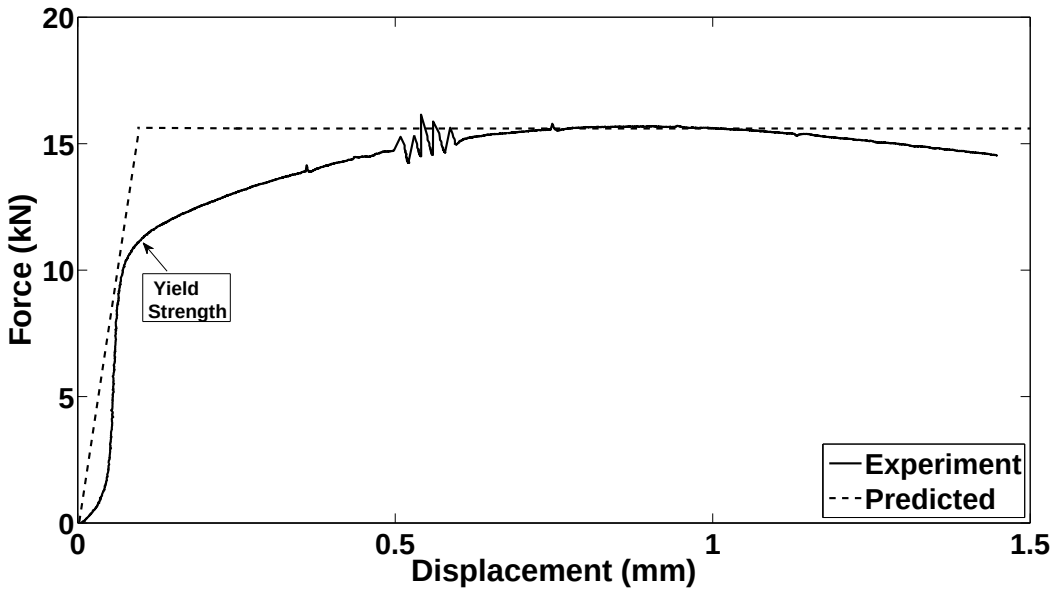


Figure 4.10: Load vs. Displacement graph of one-strut damaged 2X2 pyramidal truss core panel, specimen loaded in compression. Comparison of measured strength with predicted strength.

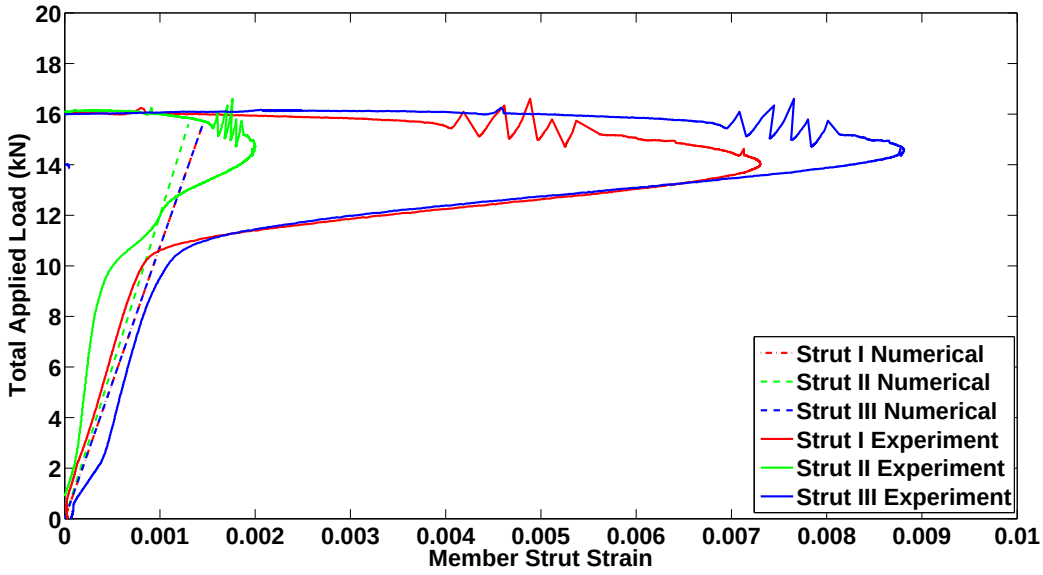


Figure 4.11: Experiment-Numerical comparison of the strains in the selected struts of the one-strut damaged 2X2 pyramidal truss core panel. Graph of applied load against the strain in the members. Specimen loaded in compression.

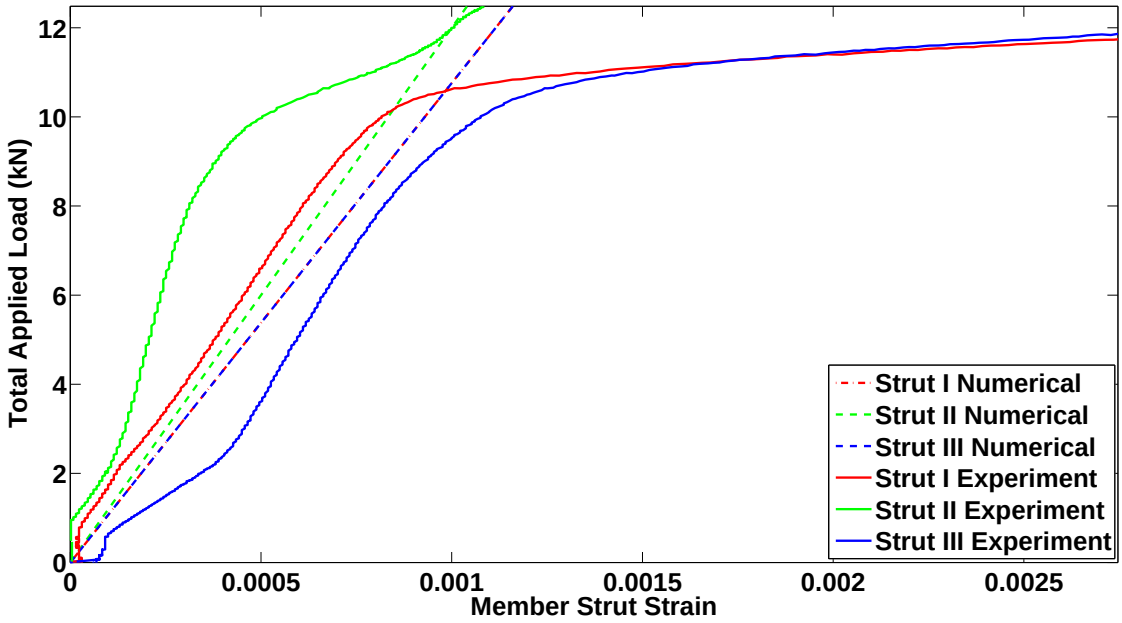


Figure 4.12: Experiment-Numerical comparison of the strains in the selected struts of the one-strut damaged 2X2 pyramidal truss core panel. Graph of applied compressive load against the strain in the members, magnified plot for clarity in comparisons.

### 4.3.2 Two-Strut and Three-Strut Damaged State Compression Experiments

For the two-strut damaged test, the damaged strut is shown in Figure 4.13 and the selected struts of interest are marked such that strut $I$ experiences maximum load at failure followed by strut $II$ and then strut $III$ as labeled in the figure. Similarly, this rank was based on the numerical predictions of the panel's behavior when those two struts are damaged. The plot of the measured macroscopic strength of the damaged panel with the numerical prediction is shown in Figure 4.14. The macroscopic load-displacement plot shows a measured failure load of 10.78 kN, which gave a strength difference of 16% when compared to the predicted failure load of 12.8 kN. The measured stiffness of the panel was 2.6 GPa, which gave a difference of 8% when compared to the predicted stiffness of 2.8 GPa. The load-strain relationship in the struts shows consistency with the numerical prediction according to the rank order of the stresses (or strains) in the struts in the region of applied load of 9.8 kN and beyond, with strut $I$ experiencing maximum strain

as expected. The main reason for the inconsistency in the preceding load region can be attributed to the profound effect of bending now seen in the compressed struts. The strut *II* (in red) was expected to be the second rank and supposed to be experiencing higher strain than strut *III* but it was undergoing bending as shown in the graphs of Figures 4.15 and 4.16. It can be seen that the effect of bending in the struts is becoming significant as further damage is introduced into the panel. This limits the validity and usefulness of the comparisons between the measured strains and the predicted strains. It also raises concern on the reliability of using the results of the measured strains under such evident bending to validate the trend of damage propagation in the panel, simply because the strain gauge on the strut should not have recorded any significant tension unless the strut was bending. For this reason, subsequent tests performed for the damaged state under compression were primarily focused on the overall macroscopic strength of the damaged panel. The damage propagation in the three-strut damaged state was based on the preceding failing struts from the two-strut damaged test and the third strut damaged to examine the effect of having three struts damaged in the same unit cell of the panel.

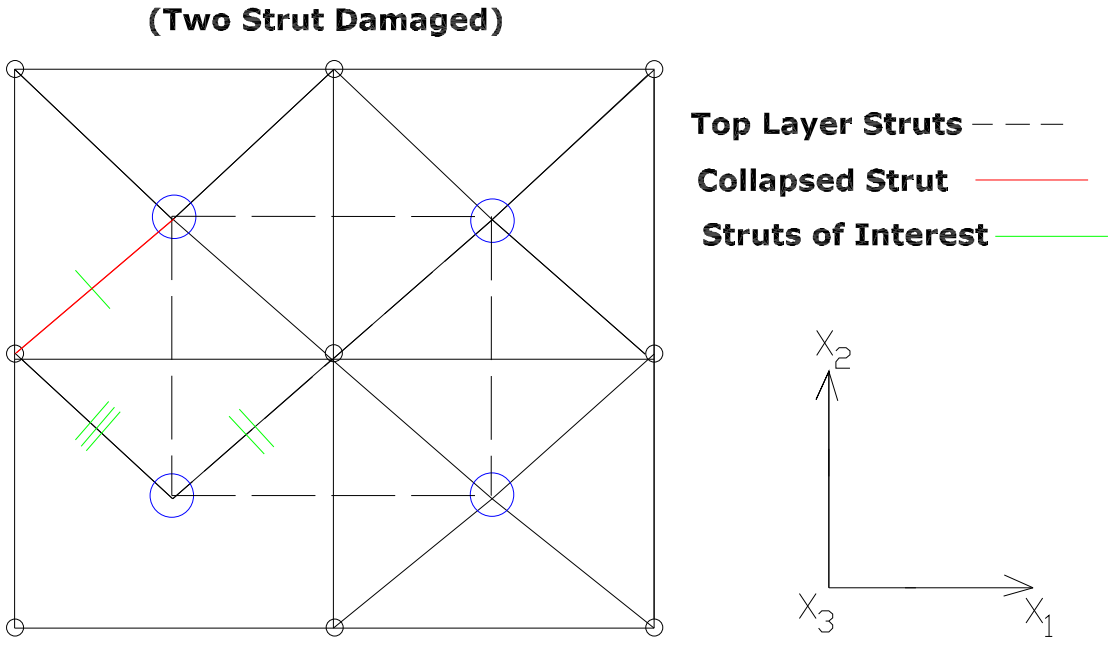


Figure 4.13: Two-strut damaged 2X2 panel loaded in compression. Damaged struts shown as the missing struts in the bottom-left cell and the Roman numerics denote the three struts of interest. The predicted failing strut is shown in red while the blue circles denote the loading in compression.

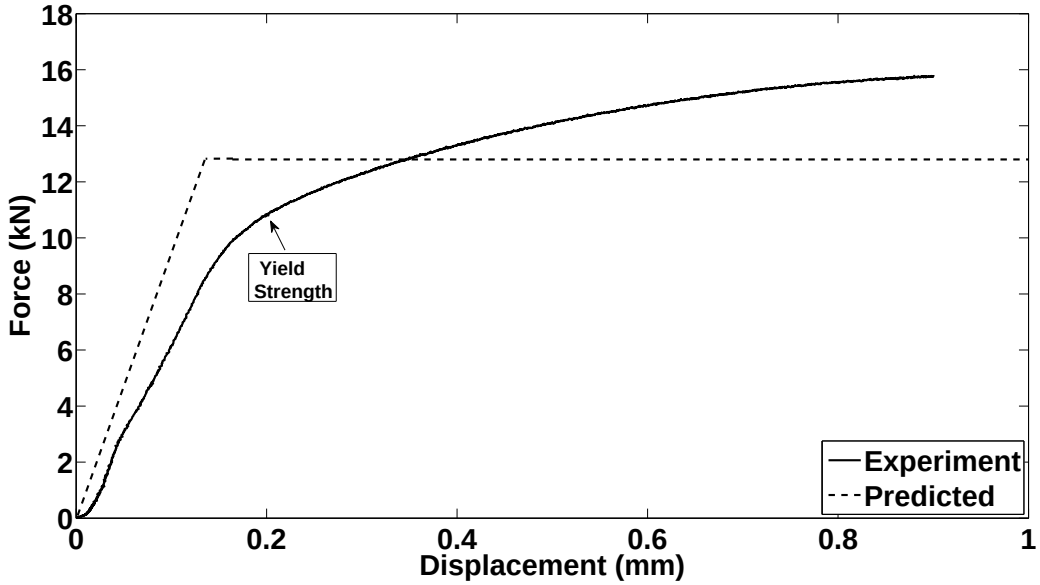


Figure 4.14: Load vs. Displacement graph of two-strut damaged 2X2 pyramidal truss core panel, specimen loaded in compression. Comparison of measured strength with predicted strength.

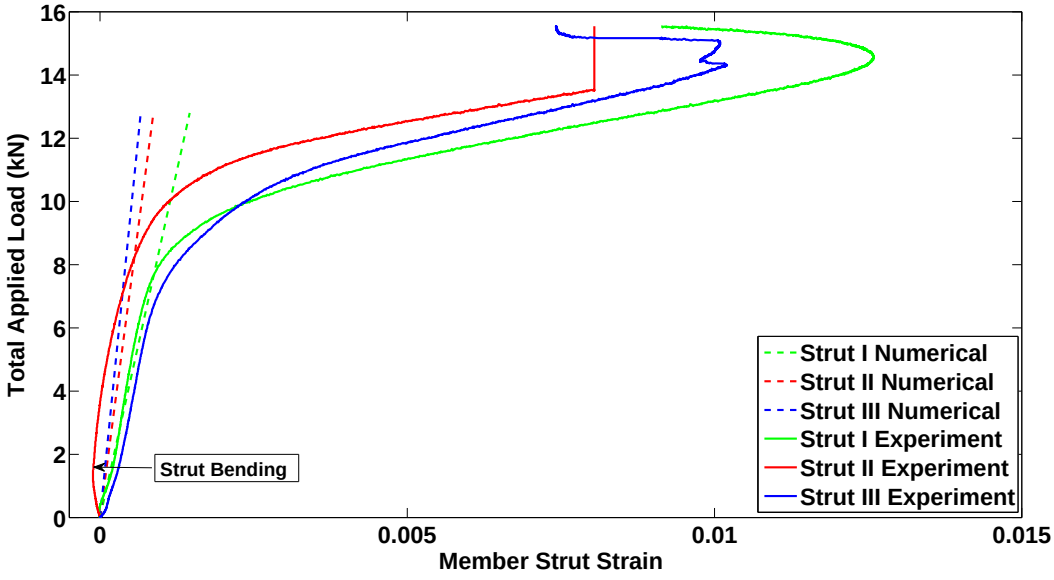


Figure 4.15: Experiment-Numerical comparison of the strains in the selected struts of the two-strut damaged 2X2 pyramidal truss core panel. Graph of applied load against the strain in the members. Specimen loaded in compression.

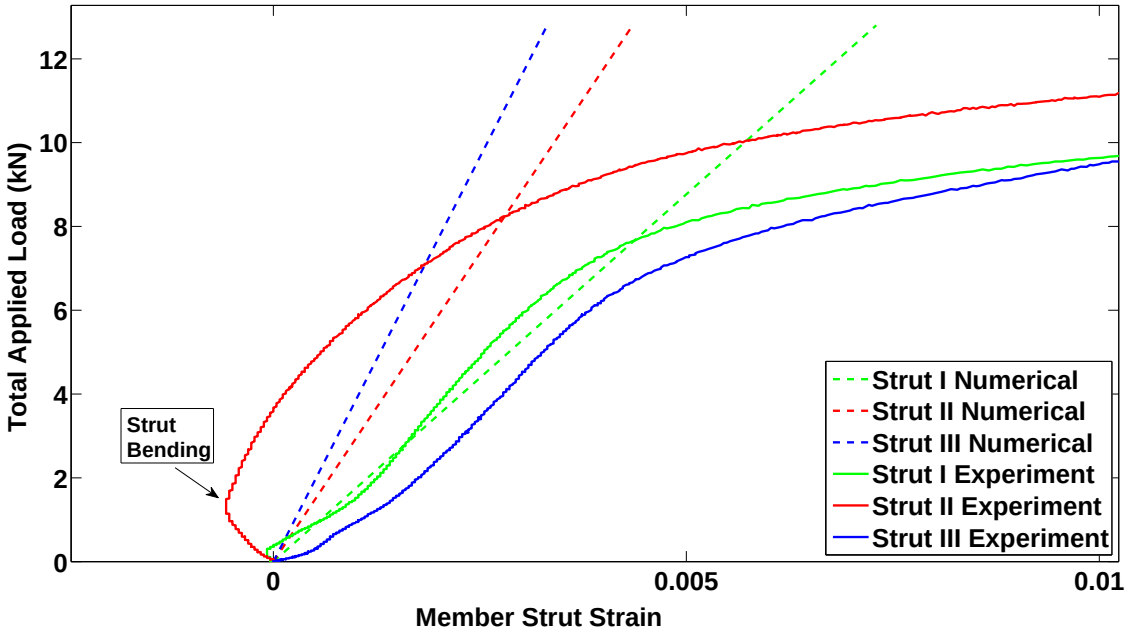


Figure 4.16: Experiment-Numerical comparison of the strains in the selected struts of the two-strut damaged 2X2 pyramidal truss core panel. Graph of applied compressive load against the strain in the members, magnified plot for clarity in comparisons.

In the three-strut damaged test, the damaged struts are shown in Figure 4.17. The load-displacement plot of the three-strut damaged state experiment along with the numerical prediction for the macroscopic strength of the panel are shown in Figure 4.18. The measured failure load was 10.9 kN, which gave a strength difference of 17.4% when compared to the predicted failure load of 13.2 kN. The measured stiffness was 3.5 GPa, which gave a difference of 2.5% when compared to the predicted stiffness of 3.6 GPa.

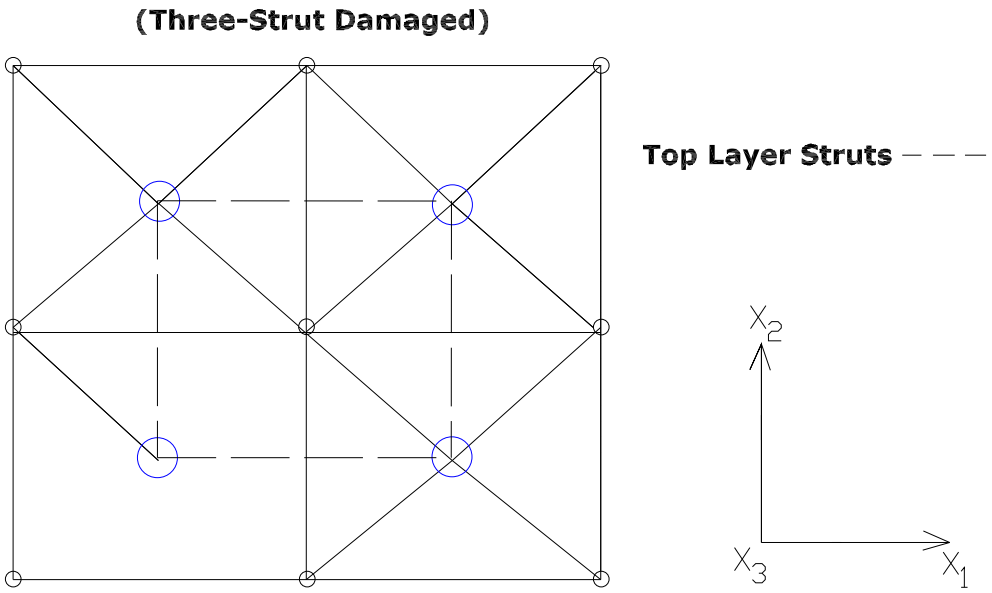


Figure 4.17: Three-strut damaged 2X2 panel loaded in compression. Damaged struts shown as the missing struts in the bottom-left cell.

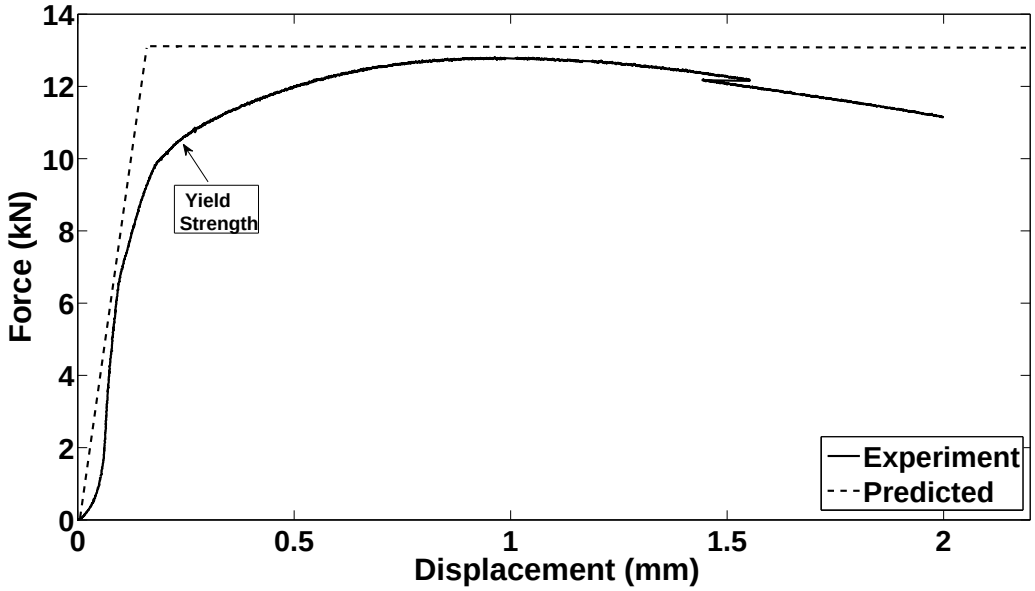


Figure 4.18: Load vs. Displacement graph of three-strut damaged 2X2 pyramidal truss core panel, specimen loaded in compression. Comparison of measured strength with predicted strength.

### 4.3.3 Shear Experiment

Shear tests were performed on damaged samples of 2.5X2.5 unit cell pyramidal truss core panels for the purpose of comparing the predicted damaged state strength to the measured strength from experiments. The test preparation and setup are identical to the procedures detailed in Section 3.5 and the first set of shear tests were carried out on an undamaged specimen, having the same geometry and mechanical properties as the specimen used in Section 3.5. The loading of the specimens in the experiments was performed by applying displacements to shear the panel through the apex nodes. In both experiment and numerical analysis, one end of the panel face sheet was constrained while displacements were applied through the other end. Because of the experience from the experiments of Subsection 4.3.1 in relation to the bending effect of compressed struts, the focus of the damaged state experiments in shear was on the struts in tension. The exception to this is that the magnitude of the stresses in each strut will not be the same once damage is inflicted on the panel. This way, reliable comparisons can be made between the measured strains of the struts and the numerical predictions. To begin, an experiment with an undamaged sample was carried out to determine which strut collapses first. Three struts in tension were chosen from three different unit cells as denoted with Roman numerals in Figure 4.19. Although it was predicted that the strains in the set of selected struts would have the same response to shear loading, it was necessary to measure the response of the selected struts to identify which strut to damage first. For the macroscopic strength of the panel, the measured failure load and the predicted failure load are plotted in Figure 4.20. The measured failure load was 6.7 kN, which gave a strength difference of 22.5% when compared to the predicted load of 8.7 kN. The measured stiffness of the panel was 1.20 GPa, which gave a difference of 13% when compared to the predicted stiffness of 1.38 GPa. The measured strains in the struts and the predicted strains are shown in Figures 4.21 and 4.22.

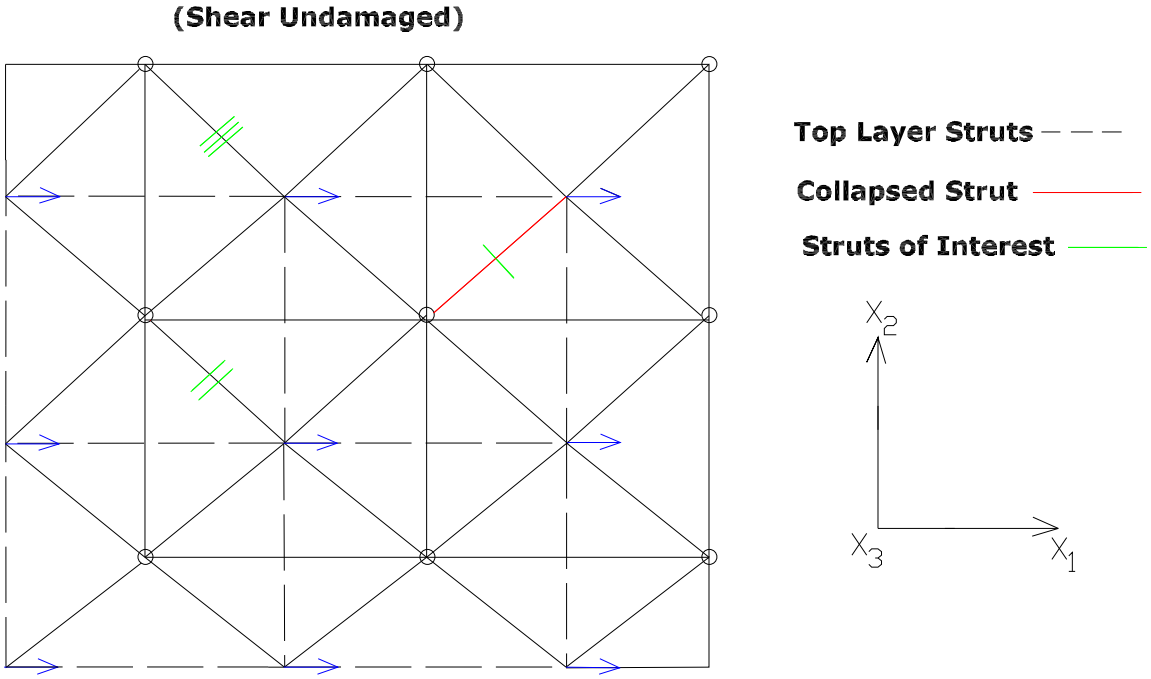


Figure 4.19: Undamaged 2.5X2.5 panel loaded in shear. The Roman numerics denote the three struts of interest. The failing strut is shown in red while the blue arrows denote the direction of loading. Top layer struts are represented with dashed lines

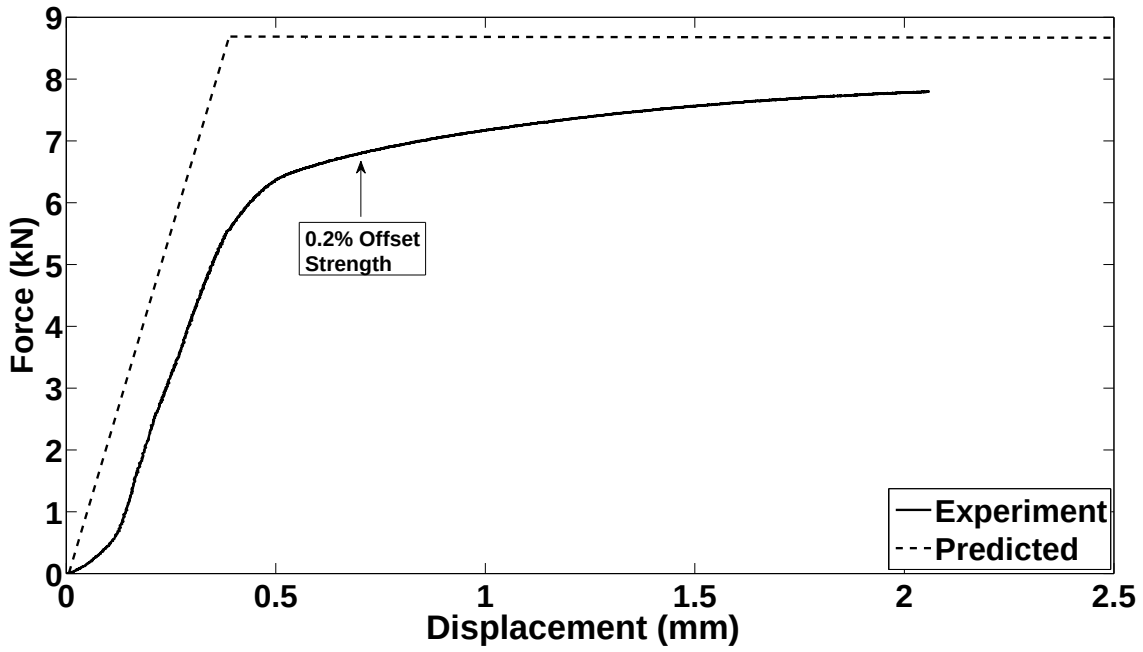


Figure 4.20: Load vs. Displacement graph of undamaged 2.5X2.5 pyramidal truss core panel, specimen loaded in shear. Comparison of measured strength with predicted strength.

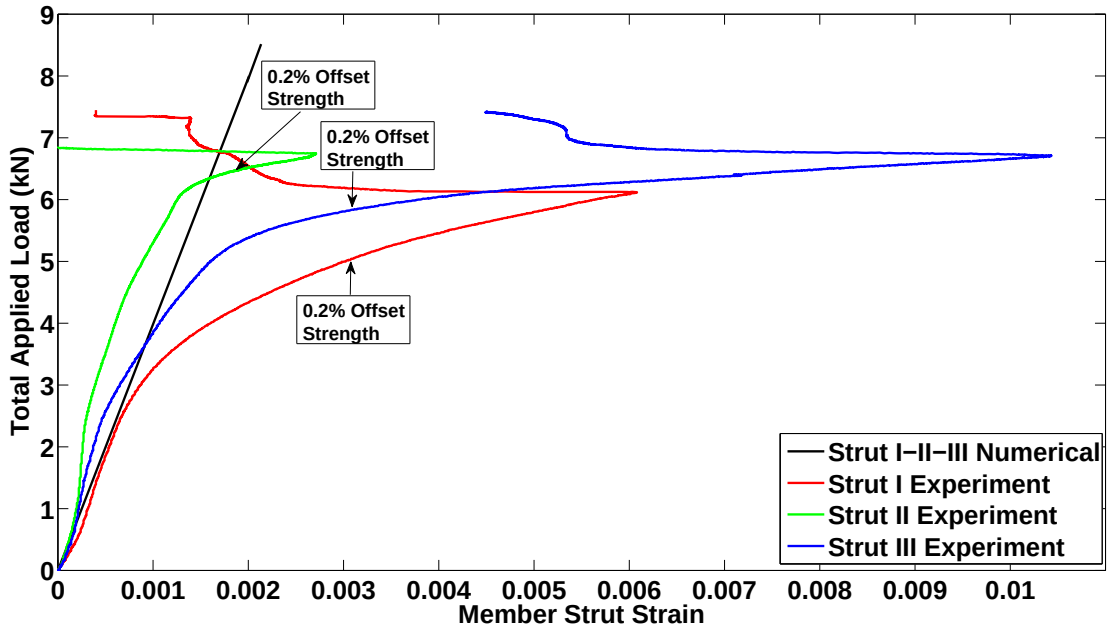


Figure 4.21: Experiment-Numerical comparison of the strains in the selected struts of the undamaged 2.5X2.5 pyramidal truss core panel. Graph of applied load against the strain in the members. Specimen loaded in shear.

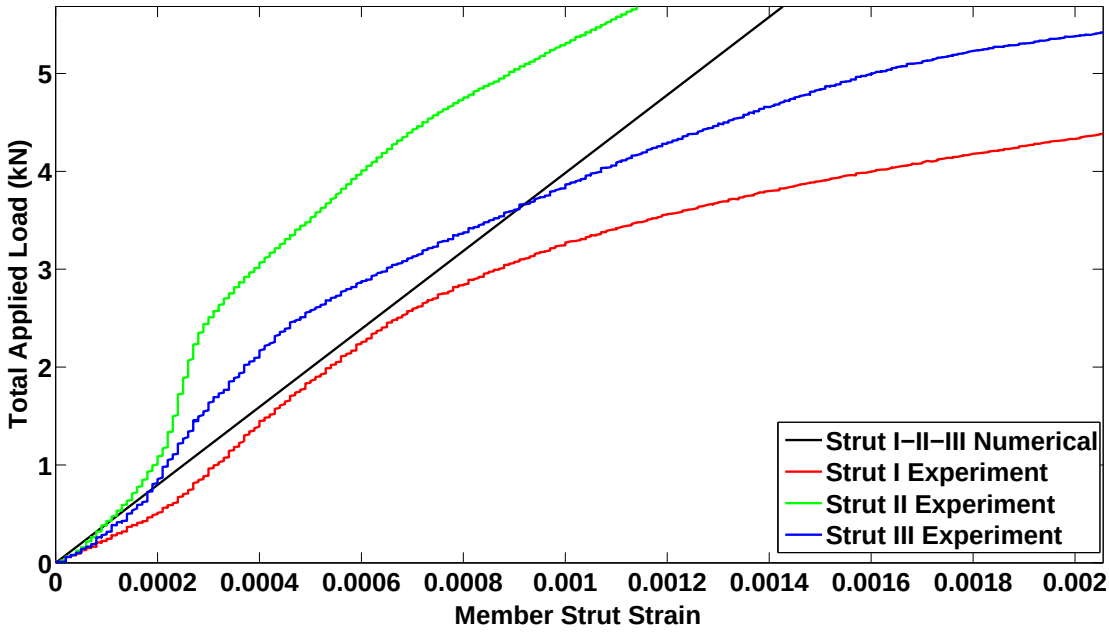


Figure 4.22: Experiment-Numerical comparison of the strains in the selected struts of the undamaged 2.5X2.5 pyramidal truss core panel. Graph of applied load against the strain in the members, magnified plot for clarity in comparisons.

The collapsed strut from the undamaged panel is shown in red, and this was the strut damaged to have the one-strut damaged panel as shown in Figure 4.23. Figure 4.24 shows the measured failure load and the predicted failure load. The measured failure load was 4.9 kN, which gave a strength difference of 18.3% when compared to the predicted load of 6 kN. The measured stiffness of the panel was 1.12 GPa, which gave a difference of 12.5% when compared to the predicted stiffness of 1.28 GPa. The measured strains and predicted strains are plotted in Figures 4.25 and 4.26. From the one-strut damaged test, the results show that the behavior of the struts is consistent with the predicted order of failure because the struts follow the same rank order as the numerical calculations. The predicted collapsed strut is consistent with the strut experiencing maximum strain as measured from the experiment. The order of the measured strain follows the same pattern as the numerical analysis.

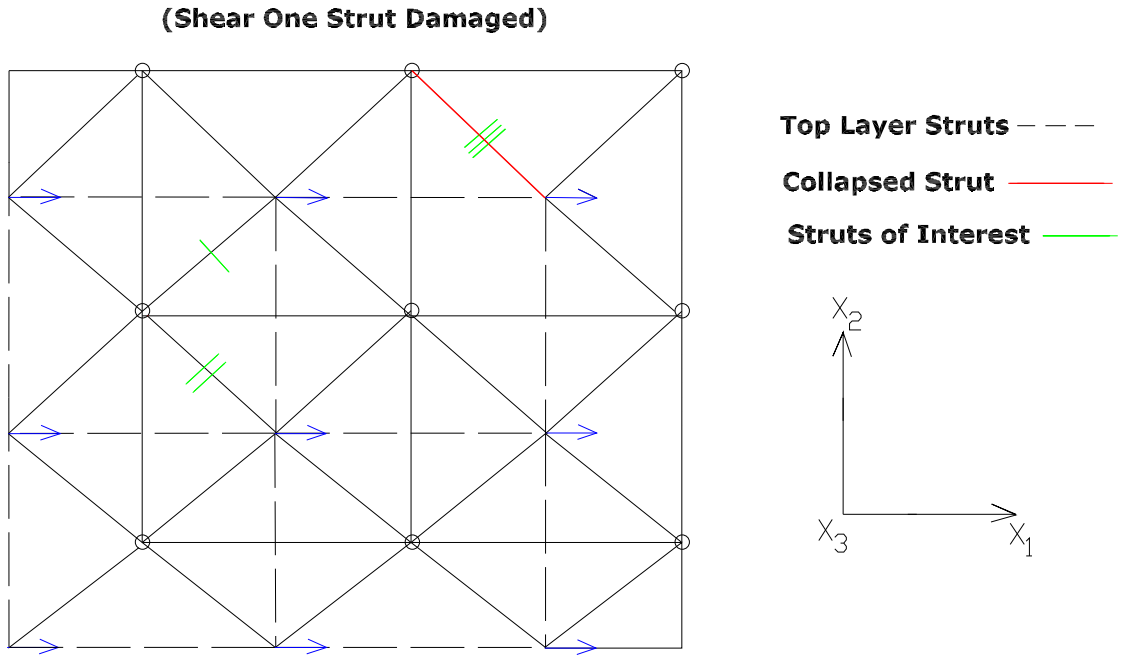


Figure 4.23: One-strut damaged 2.5X2.5 panel loaded in shear. The Roman numerics denote the three struts of interest. The failing strut is shown in red while the blue arrows denote the direction of loading. Top layer struts are represented with dashed lines

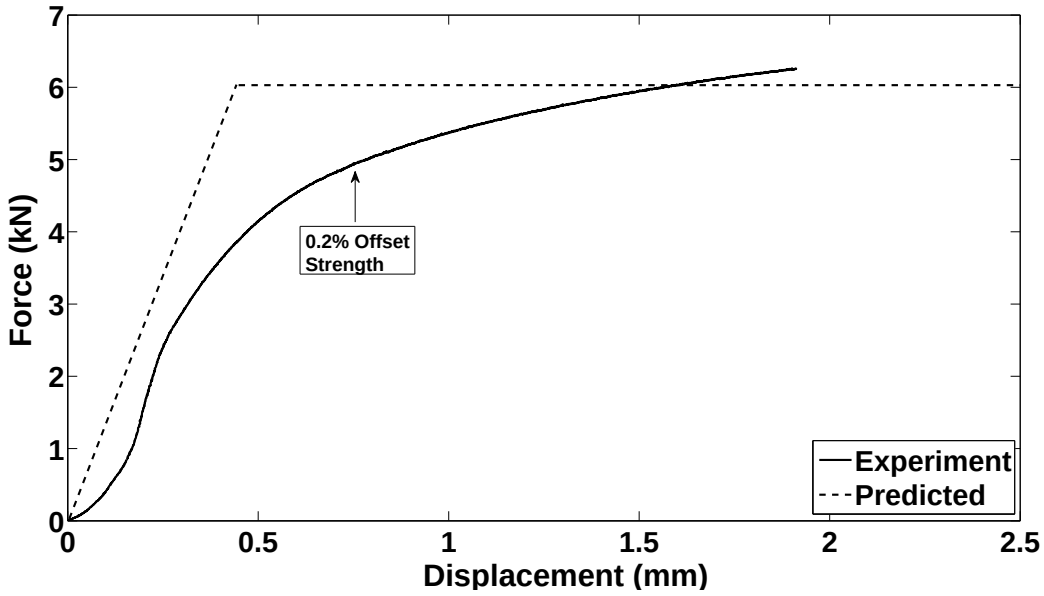


Figure 4.24: Load vs. Displacement graph of one-strut damaged 2.5X2.5 pyramidal truss core panel, specimen loaded in shear. Comparison of measured strength with predicted strength.

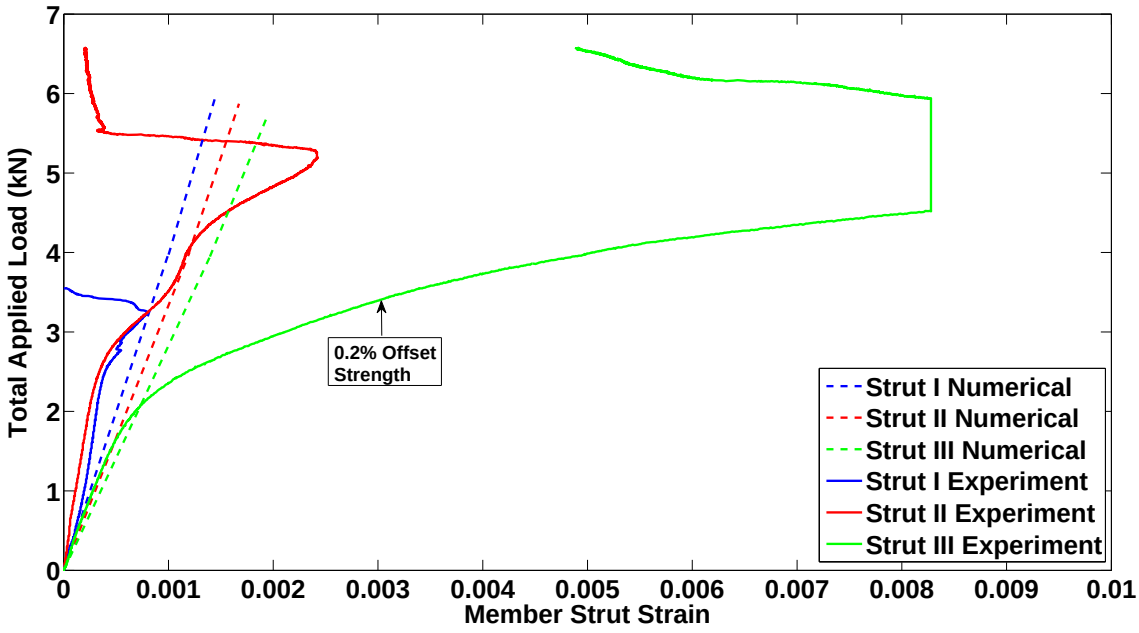


Figure 4.25: Experiment-Numerical comparison of the strains in the selected struts of the one-strut damaged 2.5X2.5 pyramidal truss core panel. Graph of applied load against the strain in the members. Specimen loaded in shear.

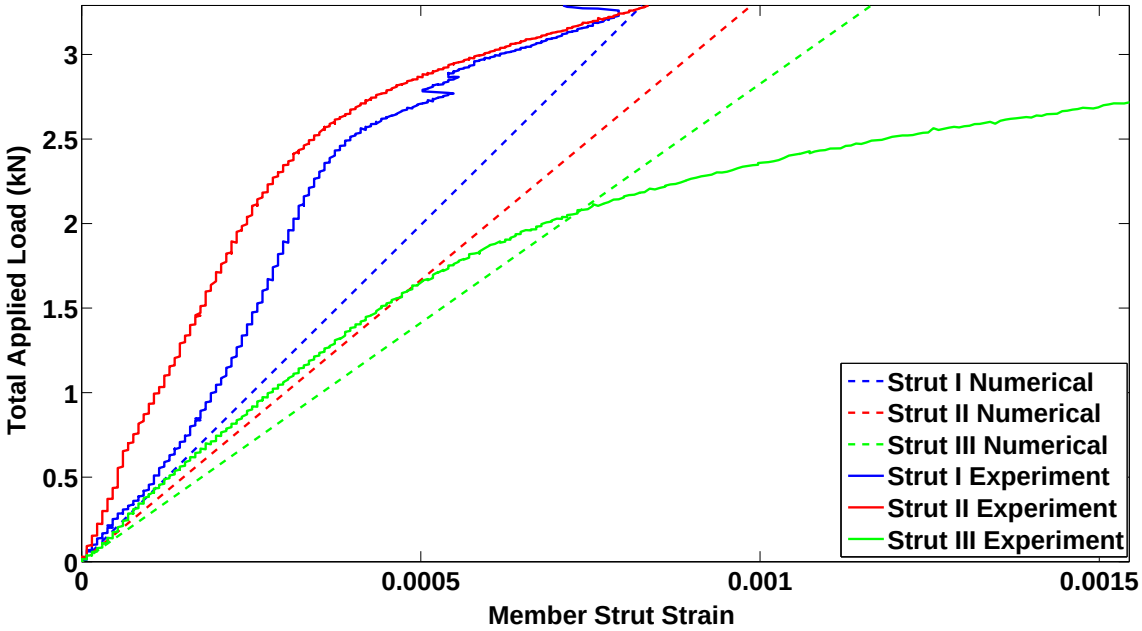


Figure 4.26: Experiment-Numerical comparison of the strains in the selected struts of the one-strut damaged 2.5X2.5 pyramidal truss core panel. Graph of applied load against the strain in the members, magnified plot for clarity in comparisons.

For the two-strut damaged test, the damaged struts from the results of the preceding damaged states are shown in Figure 4.27. The plot of the measured failure load and the predicted failure load is shown in Figure 4.28. The measured failure load was 4.6 kN, which gave a strength difference of 19.3% when compared to the predicted failure load of 5.7 kN. The measured stiffness of the panel was 0.83 GPa, which gave a difference of 9.8% when compared to the predicted stiffness of 0.92 GPa. The results from the measured strain in the struts show inconsistency with the predicted rank order of failure. The reason for the inconsistency can be attributed to the earlier mentioned effects of bending in the struts. Figures 4.29 and 4.30 show the comparisons in the strains.

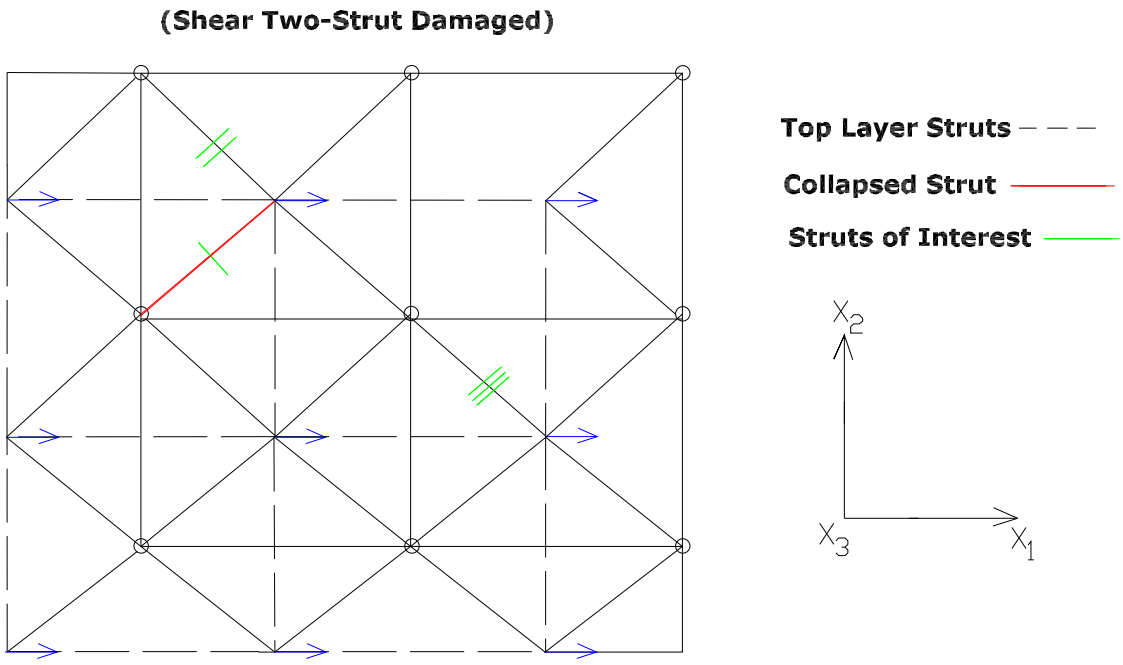


Figure 4.27: Two-strut damaged 2.5X2.5 panel loaded in shear. The Roman numerics denote the three struts of interest. The failing strut is shown in red while the blue arrows denote the direction of loading. Top layer struts are represented with dashed lines

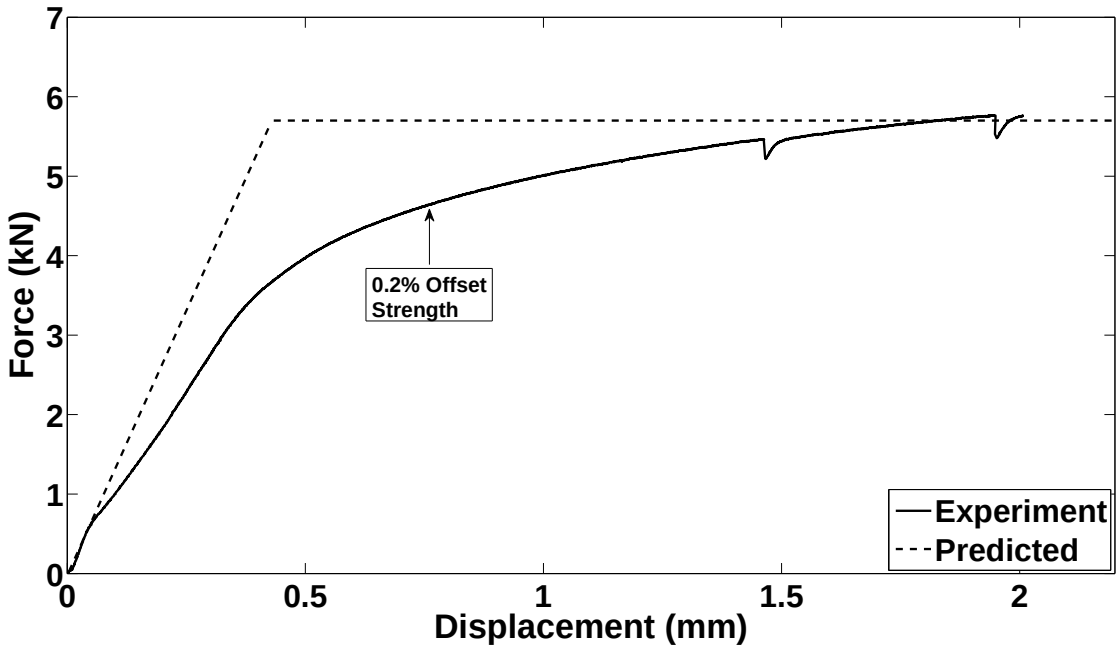


Figure 4.28: Load vs. Displacement graph of two-strut damaged 2.5X2.5 pyramidal truss core panel, specimen loaded in shear. Comparison of measured strength with predicted strength.

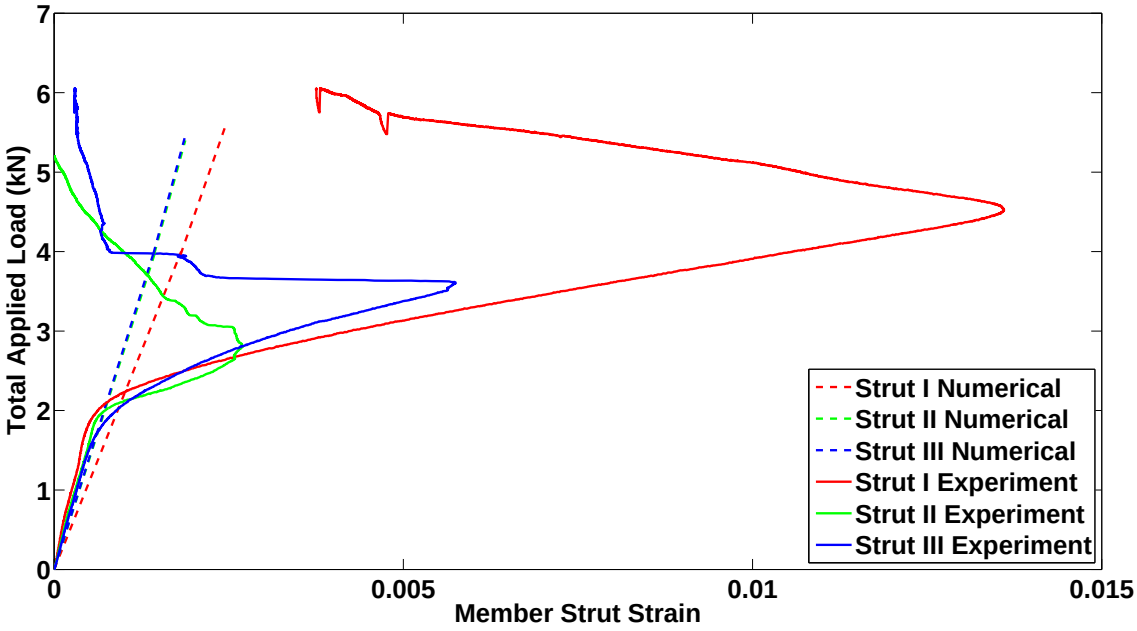


Figure 4.29: Experiment-Numerical comparison of the strains in the selected struts of the two-strut damaged 2.5X2.5 pyramidal truss core panel. Graph of applied load against the strain in the members. Specimen loaded in shear.

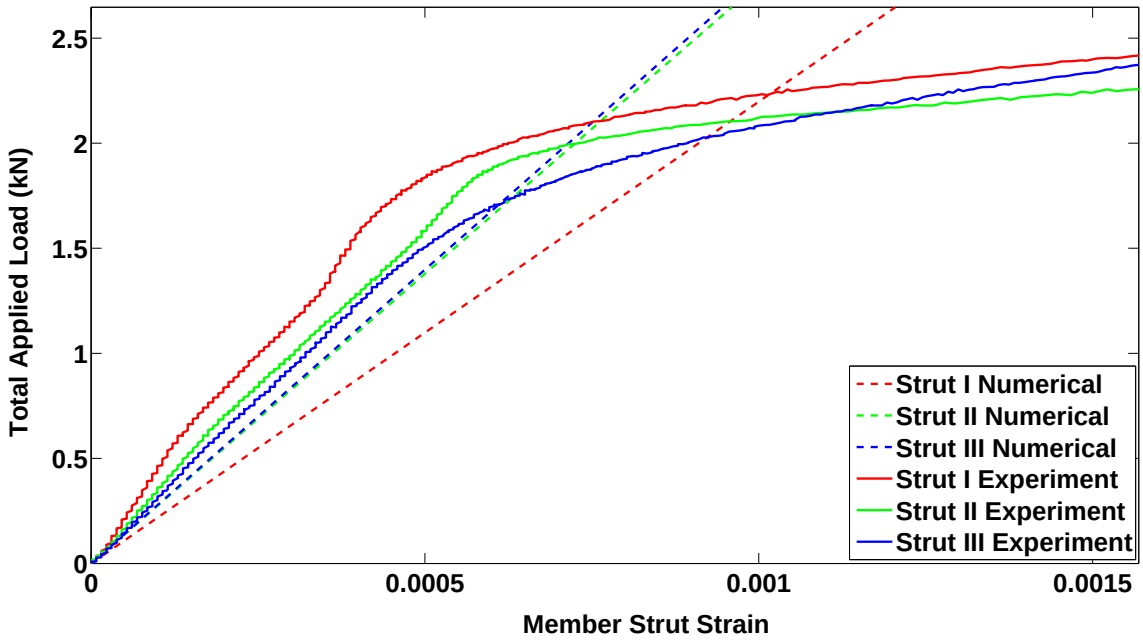


Figure 4.30: Experiment-Numerical comparison of the strains in the selected struts of the two-strut damaged 2.5X2.5 pyramidal truss core panel. Graph of applied load against the strain in the members, magnified plot for clarity in comparisons.

The three-strut damaged state is shown in Figure 4.31 following the collapsed struts in the preceding experiments of one-strut and two-strut damaged states. Figure 4.32 shows the measured failure load to the predicted failure load. The measured failure load was 3.8 kN, which gave a strength difference of 19% when compared to the predicted load of 4.7 kN. The measured stiffness was 0.78 GPa, which gave a difference of 9.3% when compared to the predicted stiffness of 0.86 GPa. The comparisons between the measured strains and predicted strains are shown in Figures 4.33 and 4.34. The results show consistency with the predicted trend of damage propagation, with the selected struts following the predicted order of failure as the numerical analysis.

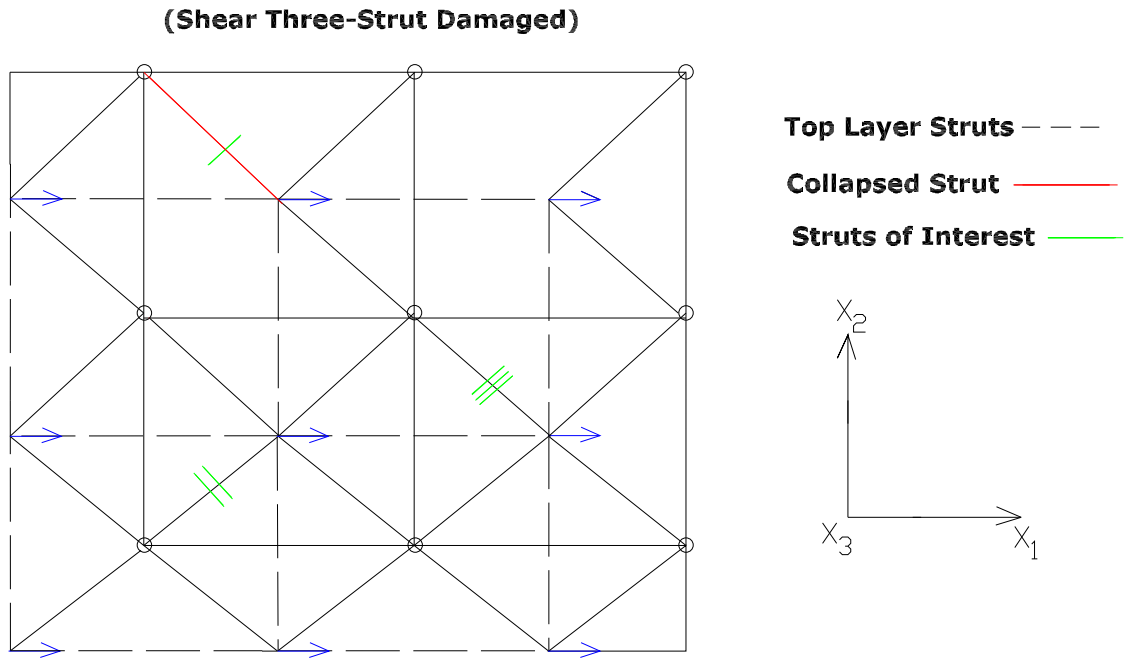


Figure 4.31: Three-strut damaged 2.5X2.5 panel loaded in shear. The Roman numerics denote the three struts of interest. The failing strut is shown in red while the blue arrows denote the direction of loading. Top layer struts are represented with dashed lines

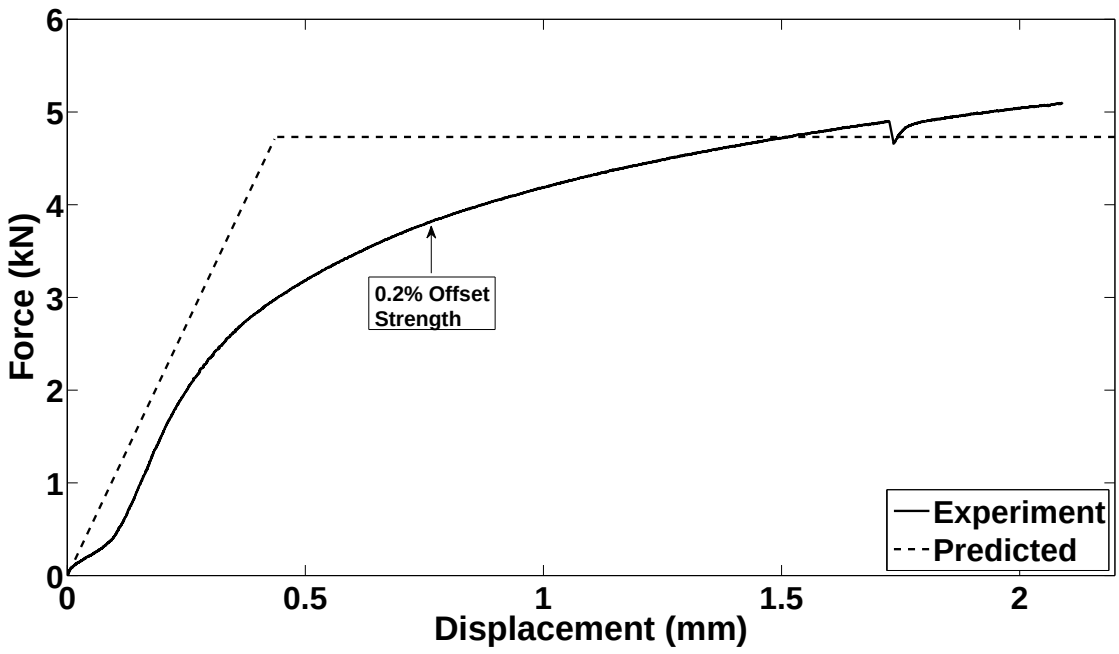


Figure 4.32: Load vs. Displacement graph of three-strut damaged 2.5X2.5 pyramidal truss core panel, specimen loaded in shear. Comparison of measured strength with predicted strength.

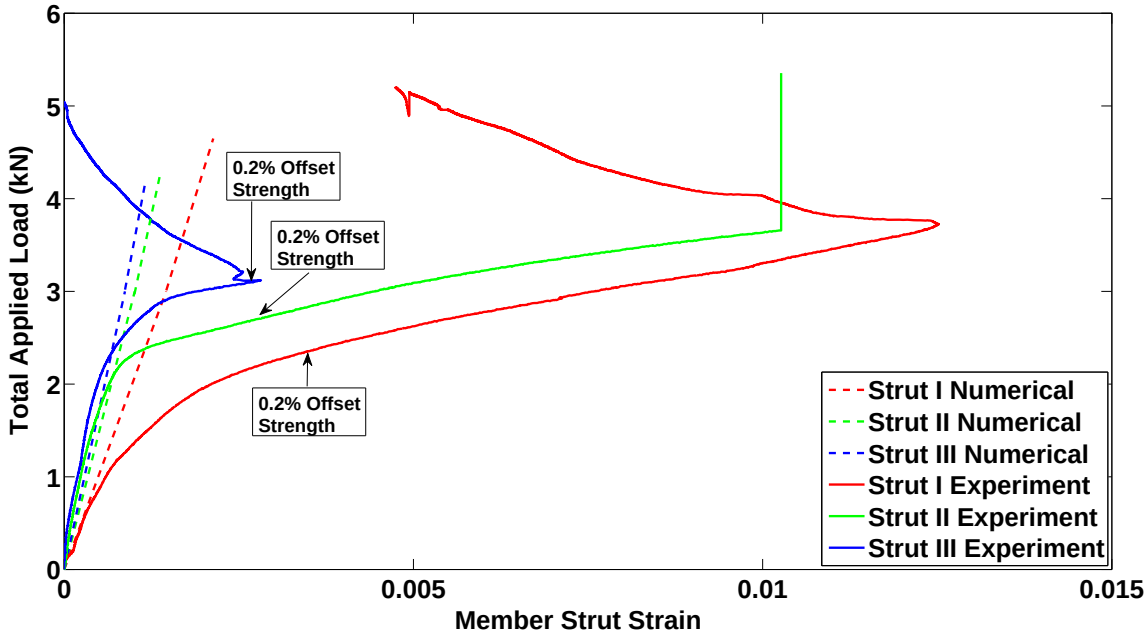


Figure 4.33: Experiment-Numerical comparison of the strains in the selected struts of the three-strut damaged 2.5X2.5 pyramidal truss core panel. Graph of applied load against the strain in the members. Specimen loaded in shear.

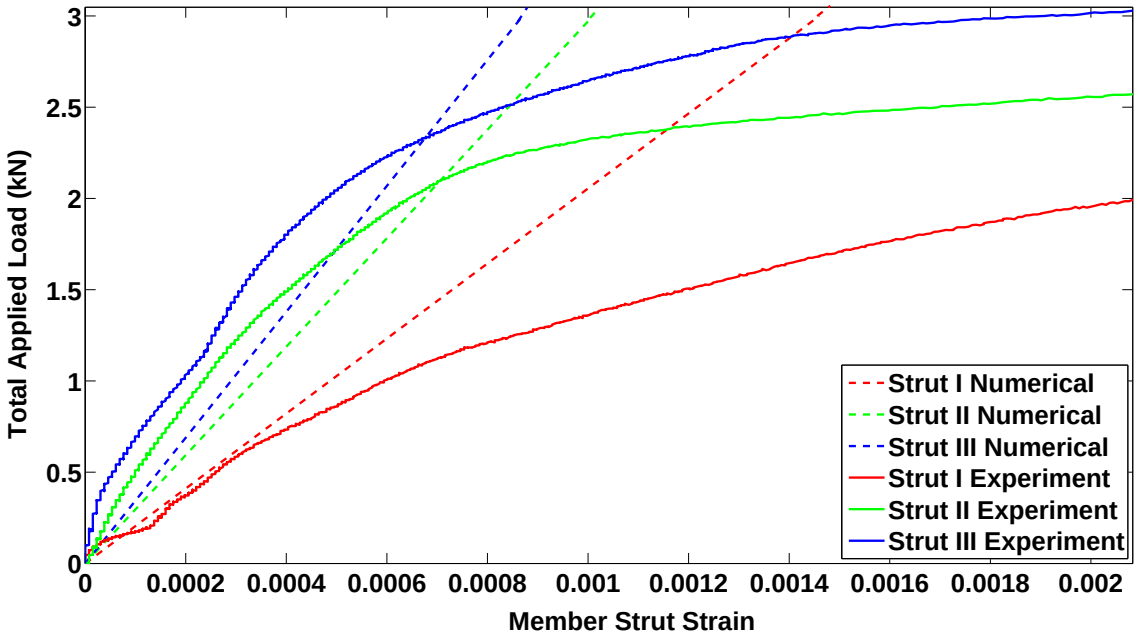


Figure 4.34: Experiment-Numerical comparison of the strains in the selected struts of the three-strut damaged 2.5X2.5 pyramidal truss core panel. Graph of applied load against the strain in the members, magnified plot for clarity in comparisons.

### 4.3.4 Summary of the Damaged State Comparisons

The damage propagation in the three-strut damaged state of compression was based on the preceding failing struts from the two-strut damaged test and the third strut intentionally damaged to examine the effect of having three struts damaged entirely in the same unit cell of the panel. The damaged experiments in shear follow the same damage pattern as the prediction. From the results of the damaged state comparisons, it is possible to represent the degradation of the panel strength in non-dimensional axes expressed in terms of $(\sigma_{33}/\sigma_y)$ for normal stresses and $(\sigma_{13}/\sigma_y)$ shear strength. The differences between the predicted damaged state strength in comparison to the measured strength are represented in the two-dimensional normalized stress space shown in Figure 4.35. The corresponding comparisons and the percentage difference between the predicted (numerical) strength of the panel to the measured strength are detailed in Table 4.2. The table shows a complete overview of the numerical-experimental strength degradation comparisons.

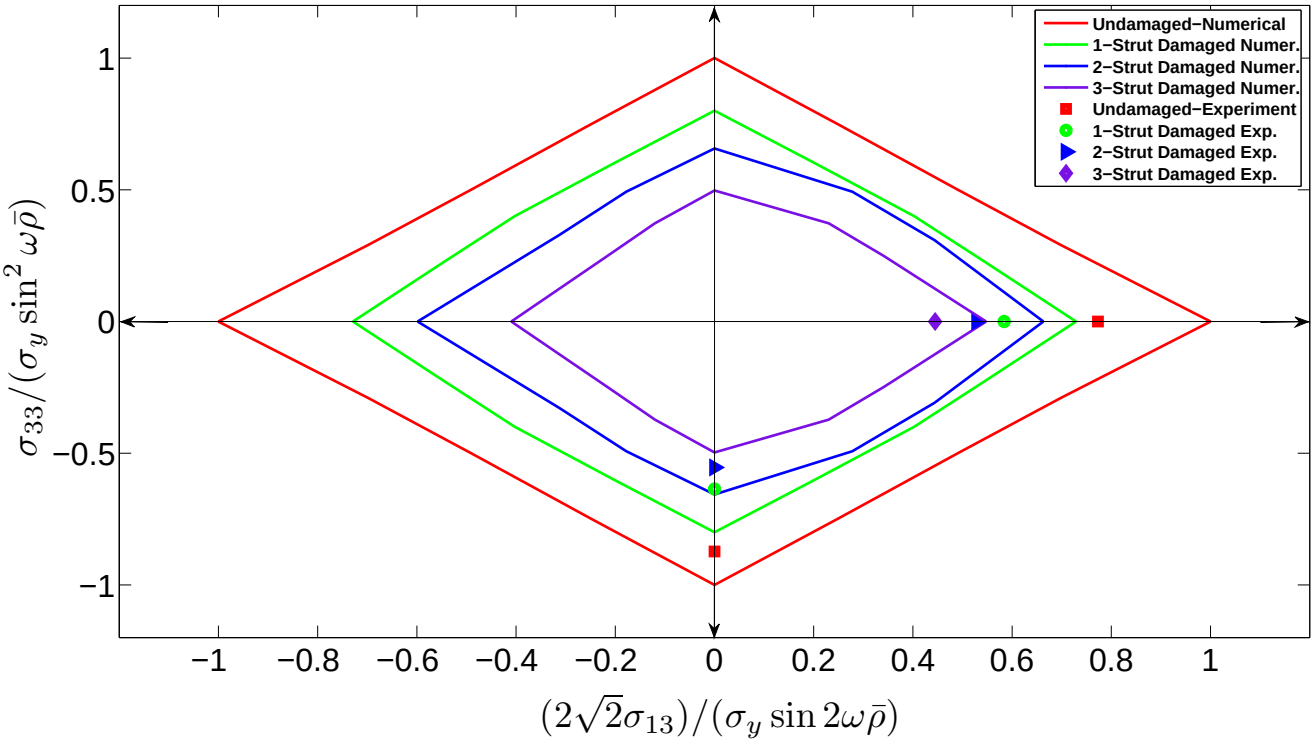


Figure 4.35: Compression and shear comparisons of experiments to numerical failure surfaces. The comparison for compression was shown up to two-strut damaged state. The third strut damaged in compression for the three-strut damaged state was to examine the effect of having three struts damaged entirely in the same unit cell, it was not from the numerical damage trend.

Table 4.2: Numerical-Experimental: Strength Comparison in Pure Shear & Compression

| | Shear (Numer.), MPa | Shear (Exp.), MPa | % of Exp. from Prediction, Shear | Compres. (Numer.), MPa | Compres. (Exp.), MPa | % of Exp. Prediction, Compres. |
|---|---|---|---|---|---|---|
| Undamaged | 5.92 | 4.6 | 77.5 | 13.09 | 11.04 | 84 |
| One-Strut Damaged | 4.25 | 3.4 | 80 | 10.5 | 8.4 | 80 |
| Two-Strut Damaged | 3.87 | 3.12 | 80.6 | 8.62 | 7.3 | 84.5 |
| Three-Strut Damaged | 3.23 | 2.6 | 80.5 | 8.9 | 7.4 | 83 |

# Chapter 5

# Conclusions

## 5.1 Fabrication Flaws

From the studies carried out in Section 3.3, it was clear that fabrication flaws contributed to the varying cross-sectional area in the struts of the specimens. This variation is one of the reasons why the measured strength from the experiments is less than the predicted strength, by approximately 20% in both compression and shear. The predicted strengths are calculated from numerical models having identical struts with their cross-sectional area taken to be the value of the strut area at 63.2% in accordance with Weibull analysis. But owing to the deviations calculated in Section 3.3, the struts of the experimental samples vary from the strut area used for the numerical calculations. This deviation contributed to the differences recorded in the macroscopic strength of the panel when compared to the prediction. Another reason for these discrepancies is the lack of perfect parallelism of the face sheets; some of the struts were more highly loaded than others. The primary goal of the damaged state experiments was to compare the residual strength of the panel in the damaged state to the predicted strength, and as well investigate the trend of damage propagation by comparing the predicted failing struts to the struts failing during the experiments. It can be seen from Subsection 4.3.3 that if the effects of bending in the struts are adequately avoided by focusing on the struts in tension, fabrication flaws do not affect the predicted behavior of the panel in terms of the trend of damage propagation. The effects of fabrication flaws do, however, affect the comparisons between the measured strains of struts of interest and the predicted strains.

## 5.2 Validation of Predicted Strength

In Chapter 2, the analytical strength of truss core sandwiches has been predicted and the numerical approach discussed. The failure surfaces were generated, and a program for calculating the strength of damaged truss core panels was developed. The measured compressive and shear strength from the experimental tests show agreement with the analytical and numerical predictions for the pyramidal truss core investigated. The comparisons of the predicted strength to the measured strength are shown in Section 3.6 for the undamaged panel and results show both shear and compressive strength to be consistently 20% less than the predicted for all damages. One of the factors for these discrepancies can be attributed to the lack of perfect parallelism between the face sheets of the tested sample, resulting in some struts to be more highly loaded than others. Another factor as discussed in Section 5.1 are the flaws in the manufacturing process, which makes the unit cells not perfectly identical. These factors are some of the reasons for the differences recorded in the experimental results when compared to the analytical and numerical predictions. However, the experiments provided the basis for using the numerical calculations for the strength of the panel in the damaged state. The above factors are some of the major limitations of using this numerical approach to calculate the strength degradation of the panel.

## 5.3 Numerical Strength Degradation

The numerical calculations of the panel strength in the damaged state were shown in Section 4.2 and results show the degradation of the panel overall strength under different levels of damage. For the damage analysis in compression, results show approximately 18% degradation in strength from the undamaged state to the one-strut damaged state, followed by 38% degradation in strength after two-strut damage, and about 50% degradation as the third strut was damaged. This pattern of strength degradation can be attributed to the effects of the missing struts associated with the unit cells where damage occurred. The damaged struts result in further load redistribution in the remaining struts of the panel, making the struts left after damage more heavily loaded and thus resulting in macroscopic degradation of the panel strength. Based on static analysis, the panel would be expected to experience a strength degradation of between 6%–25% under one strut damage, the 6% considering that damage of one of the sixteen struts in the

2X2 unit cell panel could result in strength reduction by a factor of one-sixteenth. The 25% was meant to consider that the damage of one strut from one unit cell, in the worst scenario, could render the entire unit cell damaged, thus reducing the strength of the panel by one-quarter.

The same consideration follow for the strength degradation of the panel in the case of two-strut damage, which would be expected to be 13% in the minimum estimate considering that damage of two of the sixteen struts in the 2X2 unit cell panel could result in strength reduction by a factor of two-sixteenth. A 50% strength degradation would be expected in the worst scenario if it was expected that damage of two struts from two unit cells could reduce the strength of the panel by half. For three-strut damage, the strength degradation would be expected to be 19% in the minimum estimate considering that damage of three of the sixteen struts in the 2X2 unit cell panel could result in strength reduction by a factor of three-sixteenth. A 75% strength degradation would be expected in the worst scenario if it was expected that damage of three struts from three different unit cells could reduce the strength of the panel by three-quarter. The results show that the numerical program calculates the damaged strength of the panel approximately within a region half way between range of strength degradation. For the damaged state in shear, the rate of strength degradation resulting from the damage was calculated and the residual strength of the panel after three struts damaged was about 43% of the initial strength of the undamaged panel. The panel had a strength degradation of about 27% from the undamaged state to one-strut damage state, and followed by 39% degradation in strength after two-strut damage. Also, the numerical calculations show that minimum symmetrical boundary conditions can be exploited to estimate the residual strength of large arrays of truss core sandwich panels, which allow more damage.

## 5.4 Experimental Strength Degradation

To measure the residual mechanical strength of damaged truss core panels, experiments were performed on panels subject to different levels of damage in both compression and shear. From the measured strains of the selected struts, as detailed in Section 4.3, the results show consistency in the trend of damage propagation when the effects of bending in the struts is avoided by focusing on struts in tension. For both shear and compression tests, the measured macroscopic strength in the damaged state is approximately 20% less than predicted, which is consistent with the difference recorded in the undamaged state.

The results show a consistent pattern of strength overprediction for each level of damage, as shown in Table 4.2. The results from the experiments show that the strength of the panel in the damaged state closely replicates the predicted strength. The experiments provide validation for using the numerical program for analyzing complex failure mechanisms involving the interactions between multiple unit cells and the residual effects of strut failure in larger arrays of truss core sandwich panels. With such a computational solution, the strength of arrays of multiple unit cells can be calculated and the damaged panel strength can be attained. One way to limit the differences in the results would be to fabricate the panel such that it has fewer fabrication flaws as investigated by Queheillalt et al [22], where an extrusion and electro-discharge machining (EDM) method was used to manufacture a panel more close to the analytical model.

## 5.5 Recommendations for Future Research

For future work on research involving damage and damage propagation in truss core sandwiches, it might be interesting to consider the following:

(i) Having shown the possibilities and limitations of using the numerical program to calculate the residual strength of truss core sandwiches under mechanical loading, it might be interesting to expand the numerical program to consider larger arrays of unit cells, automating damage in the panel based on the method of eliminating the failing strut at each iteration, while following the yielding-buckling failure criterion.

(ii) Experimentation on truss core sandwiches under fatigue, rather than just static loading. This would better represent the failure behavior and damage propagation of the panel under mechanical loading in a manner more representative of actual use.

(iii) A broader consideration of how other factors such as corrosion, impact loading or blast contribute to damage in truss core sandwiches, and how these factors inter-relate with the failure behavior or damage propagation under mechanical loading when in use. This would be a more robust approach to considering all the factors which the panel is exposed to in service, and which all have the possibilities of contributing to its strength degradation.

# Bibliography


[1] T. Bitzer, "Honeycomb Technology," 1997. Chapman & Hall, London.

[2] HexWeb, "Honeycomb Attributes and Properties," 1999. Publication No. TSB 120, Hexcel Composites, Hexweb Inc. Pleasanton.

[3] L. J. Gibson and M. F. Ashby, "Cellular Solids, Structure and Properties," 1997.

[4] D. J. Sypeck, "Constructed Cellular Metals," in *TMS Conference Proceedings*, pp. 35–45, The Minerals, Metals & Materials Society (TMS), 2002.

[5] M. F. Ashby, A. G. Evans, N. A. Fleck, L. J. Gibson, J. W. Hutchinson, and H. N. G. Wadley, *Metal Foams: A Design Guide*. Butterworth-Heinemann, Boston, 2000.

[6] A. G. Evans, J. W. Hutchinson, and M. F. Ashby, "Multifunctionality of Cellular Metal Systems," *Progress in Material Science*, vol. 43, p. 171, 1999.

[7] D. J. Sypeck and H. N. G. Wadley, "Multifunctional Microtruss Laminates: Textile Synthesis and Properties," *Journal of Materials Research*, vol. 16(3), p. 890, 2001.

[8] A. G. Evans, J. W. Hutchinson, N. A. Fleck, M. F. Ashby, and H. N. G. Wadley, "The Topological Design of Multifunctional Cellular Metals," *Progress in Materials Science*, vol. 46, pp. 309–327, 2001.

[9] H. N. G. Wadley, N. A. Fleck, and A. G. Evans, "Imperfection sensitivity of pyramidal core sandwich structures," *Int. J. Solids and Structures*, vol. 44, pp. 4690–4706, 2007.

[10] H. N. G. Wadley, "Multifunctional Periodic Cellular Metals," *Proc. Royal Society A*, vol. 364, pp. 31–68, 2006.

[11] J. C. Wallach and L. J. Gibson, "Truss Core Sandwich Panels and Methods for Making Same," *U.S. Patent No. 6644535*, 2003.

[12] H. N. G. Wadley, "Cellular Metals Manufacturing," *Advanced Engineering Materials, Int. J. of Solids and Structures, Special Issue*, vol. 4, no. 10, pp. 726–733, 2002.

[13] F. W. Zok, S. A. Waltner, Z. Wei, H. J. Rathbun, R. M. McMeeking, and A. G. Evans, "A protocol for characterizing the structural performance of metallic sand-

wich panels: application to pyramidal truss cores," *Int. J. of Solids and Structures*, vol. 41, pp. 6249–71, 2004.

[14] C. G. Jung, S. J. Yoon, D. Y. Yang, S. M. Lee, S. J. Na, and S. H. L. et al, "Fabrication and static bending test in ultra light inner structured and bonded (ISB) panel containing repeated pyramidal structure," *J. Korean Society Proceedings in Engineering*, vol. 22, pp. 175–82, 2005.

[15] D. J. Sypeck and H. N. G. Wadley, "Cellular metal truss core sandwich structures**," *Advanced Engineering Materials*, vol. 4, no. 10, pp. 759–64, 2002.

[16] V. Deshpande and N. Fleck, "Collapse of truss-core sandwich beams in 3-point bending," *Int. J. Solids and Structures*, vol. 38(36-37), pp. 6275–6305, 2001.

[17] V. Deshpande and M. Ashby, "Foam topology: bending versus stretching dominated architectures," *Acta Materialia*, vol. 49, p. 1035, 2001a.

[18] R. C. Hibbeler, *Structural Analysis*. Prentice Hall, 2005.

[19] MathWorks, "MATLAB," 2010. The MathWorks Natick, MA.

[20] J. C. Wallach and L. J. Gibson, "Truss Core Sandwich Panels and Methods for Making Same," *U.S. Patent No. 6644535*, 2003.

[21] R. Biagi and H. Bart-Smith, "Fabrication and Structural Performance of Periodic Cellular Metal Sandwich Structures," *Composites Science and Technology*, vol. 63, pp. 2331–2343, 2003.

[22] D. T. Queheillalt, Y. Murty, and H. N. G. Wadley, "Mechanical properties of an extruded pyramidal lattice truss sandwich structure," *Scripta Materialia*, vol. 58, pp. 76–79, 2008.

[23] F. R. Shanley, "Inelastic column theory," *Journal of the Aeronautical Sciences*, vol. 14, no. 5, pp. 261–268, 1947.

[24] ASTM, "C365 Standard Test Method for Flatwise Compressive Properties of Sandwich Cores," *ASTM International, West Conshohocken, PA*, 2006.

[25] ASTM, "C273 Standard Test Method for Shear Properties of Sandwich Core Materials," *ASTM International, West Conshohocken, PA*, 2006.

[26] R. B. Abernethy, *The New Weibull Handbook*. Library of Congress Cataloging in Publication Data, 2006.

[27] W. Weibull, "A statistical distribution function of wide applicability," *Journal of Applied Mechanics-Trans. ASME*, vol. 18, pp. 293–297, 1951.

[28] M. B. Wilk and R. Gnanadesikan, "Probability plotting methods for the analysis of data," *Biometrika Trust*, vol. 55, no. 1, pp. 1–17, 1986.

[29] W. Nelson, *Applied Life Data Analysis*. Wiley-Blackwell, 2000.